5
Electromagnetic Interactions with Solids

Ricardo Díez Muiño, Eugene E. Krasovskii, Wolfgang Schattke,
Christoph Lienau, and Hrvoje Petek

In this chapter, we discuss various processes that contribute to absorption of light at solid surfaces. We particularly focus on the optical response of metals including single-particle interband electron–hole (e-h) pair excitations, which are common to semiconductors and insulators, as well as the free-electron response, which is particular to metals and doped semiconductors. Free electrons participate both in the collective screening response and in the single-particle intraband absorption. A characteristic property of metals conferred by free electrons is the dielectric function with large negative real and small positive imaginary parts in the infrared and visible spectral regions. A time-dependent electromagnetic field incident on a metal surface at frequencies below the material-specific plasma frequency is strongly screened by the free-carrier polarization. The screening limits the penetration of the electric field to the skin depth of the metal, typically corresponding to 20–30 nm in the visible spectrum. Moreover, the coherent oscillation of free carriers with the opposite phase as the incoming field (see Section 5.4.2), as imposed by the negative real part of the dielectric function, leads to specular reflection of a π-phase-shifted field with minimal loss to e-h pair excitation. We examine the factors that define the optical properties of metals and how light deposits energy into elementary excitations at a metal surface. Absorption of light generates hot carriers within the metal bulk or at surfaces in intrinsic or adsorbate localized surface states. These excitations undergo relaxation through elastic and inelastic carrier scattering processes or induce chemistry, as discussed elsewhere in this book. The absorption of light is detected through linear or nonlinear optical spectroscopy; alternatively, it can be detected through photoelectron emission. Although both optical and photoemission measurements have the same requirements for momentum conservation in the process of photon absorption, the former confers momentum integrated information and is therefore unsuitable for band structure mapping. We discuss the optical absorption process with the object of specifying the hot electron and hole distributions in the energy and momentum space [$E(\mathbf{k})$] that are generated by absorption of light through interband and intraband transitions. These distributions are important for the secondary processes induced by hot carriers, such as femtochemistry, as well as to describe photoemission. By contrast

Dynamics at Solid State Surfaces and Interfaces: Volume 2: Fundamentals, First Edition.
Edited by Uwe Bovensiepen, Hrvoje Petek, and Martin Wolf.

to optical spectroscopy, photoemission spectroscopy has provided a wealth of information on the band structures of the occupied states of solids, and with the advent of tunable ultrafast lasers, it holds a further promise for band mapping of their unoccupied states. To this end, we describe recent theoretical proposals for the band mapping by resonant multiphoton photoemission. The coherent response of metals has been used to great advantage in the field of plasmonics. We describe the nature of localized and propagating plasmonic modes of metal surfaces, how they can be manipulated through morphology and dielectric environment, and how they couple with other excitations such as excitons in molecular aggregates.

5.1
Dielectric Function of Metals

For sufficiently low intensities, absorption of the electromagnetic radiation by a solid is described by perturbation theory; transitions between the occupied and unoccupied stationary states represent a negligible deviation of the system from its ground state. In the simplest case, when many-body interactions are described by a mean field, the probability that a photon of energy $\hbar\omega$ be absorbed is reduced to summing up the probabilities of all possible one-particle excitations for all crystal momenta **k**. The probability of each individual transition obeys the Fermi Golden Rule and, in the long-wavelength limit, the dipole selection rules [1]. In a crystal, the electron states can be chosen to be eigenstates of the translation operator, so that the non-vanishing ones are only the transitions between electron states having the same **k**. In the dipole approximation, the transition probability amplitude is given by the matrix element $M^{\mathrm{e}}_{mn}(k) = \langle \mathbf{k}n | -i\nabla_{\mathrm{e}} | \mathbf{k}m \rangle$, where ∇_{e} is the projection of the gradient operator in the direction of the electric field and m and n are the band numbers of the occupied and unoccupied Bloch states, respectively. The **k**-conserving transitions are often referred to as vertical or direct transitions, with the momentum of a photon being negligible compared to the range of momenta spanned by the Brillouin zone vectors. The total probability of being absorbed (per second and per unit volume) is given by an integral over the Brillouin zone, and it can be converted into the optical constants of the material using the macroscopic relationships of the classical electromagnetic theory [2]. A more consistent approach is to calculate the linear longitudinal response of the many-electron system within the random phase approximation (RPA). The simplest version of the RPA [3], which neglects variations in the electric field on the scale of the unit cell, leads to the same result. The imaginary part of the macroscopic dielectric function ε'' corresponding to interband transitions, which is of primary interest in this section, is then simply connected to the band structure:

$$\varepsilon''(\omega) = \frac{4\pi^2 e^2}{m^2\omega^2} \sum_{mn} \int_{BZ} \frac{2dk}{(2\pi)^3} |M^{e}_{mn}(k)|^2 \delta(E_n(k) - E_m(k) - \hbar\omega). \tag{5.1}$$

The terms $m \neq n$ result in broad absorption spectra reflecting transitions between electronic bands specific to each solid. This interband term is often referred to as the

Lorentz term and can be represented as a sum of several Lorentz oscillators corresponding to specific regions of phase space with a large joint density of initial and final states that are connected by optical transitions.

The one-particle model also describes the fundamental difference between metals and semiconductors: the normal incidence reflectivity of the former approaches unity as $\omega \to 0$. This is caused by the intraband term, $m = n$, which contributes to the optical response of metals due to the presence of the Fermi surface. In the absence of damping, the intraband term gives rise to a singularity of $\varepsilon''(\omega)$ at $\omega \to 0$:

$$\varepsilon''_{\text{intra}}(\omega) = \frac{\pi}{2}\omega_{\text{p0}}^2 \frac{\partial\delta(\omega)}{\partial\omega}. \tag{5.2}$$

The Kramers–Kronig transform of Eq. (5.2) is the Drude contribution to the real part of the dielectric function:

$$\varepsilon'_{\text{intra}}(\omega) = 1 - \frac{\omega_{\text{p0}}^2}{\omega^2}. \tag{5.3}$$

The parameter $\omega_{\text{p0}} = (4\pi ne^2/m)^{1/2}$ in Eqs. (5.2) and (5.3) is the plasma frequency of a free-electron gas, which depends entirely only on the electron density n.

The real part of the dielectric function is also seen to diverge as $\omega \to 0$, and consequently, the normal incidence reflectivity of metals R approaches unity in this limit. As long as the real part remains large and negative, the reflectivity is high; above ω_{p0}, the free electrons are no longer able to screen the external field and the metal becomes transparent. At the plasma frequency, light can propagate through a metal as a strongly damped collective charge density fluctuation [4]. In real metals, the frequencies of plasma oscillations, which occur when $\varepsilon'(\omega)$ crosses zero and $\varepsilon''(\omega)$ is small, are modified by interband transitions described by the Lorentz term. The Drude parameter ω_{p}^2 is given by the integral over the Fermi surface

$$\omega_{\text{p}}^2 = \frac{1}{\pi^2}\sum_n \int_{\text{FS}} \mathrm{d}S \left(\frac{(\mathbf{e}\cdot\mathbf{v}_n(\mathbf{k}))^2}{|\mathbf{v}_n(\mathbf{k})|} \right). \tag{5.4}$$

Here, $\mathrm{v}_n(\mathbf{k})$ is the group velocity of the Bloch state $|nk\rangle$ and the vector $\mathbf{e}$ points in the direction of polarization of the external field. Fermi surfaces of realistic metals have very complicated shapes, so the actual values of ω_{p}^2 are usually much smaller than the free electron result ω_{p0}^2.

5.1.1
Calculations of Dielectric Functions

The one-particle approach provides a simple scheme for calculating optical properties with *ab initio* methods of band theory. In the majority of applications, the solutions of the Kohn–Sham equations of the density functional theory are used for $|\mathbf{k}m\rangle$ and $E_m(\mathbf{k})$. For metals, this usually leads to a satisfactory agreement with experiment. The typically high quality of the above approach is illustrated in Figure 5.1a for platinum (Pt): below 30 eV, the measured optical spectra [5] are well described by the theory [6].

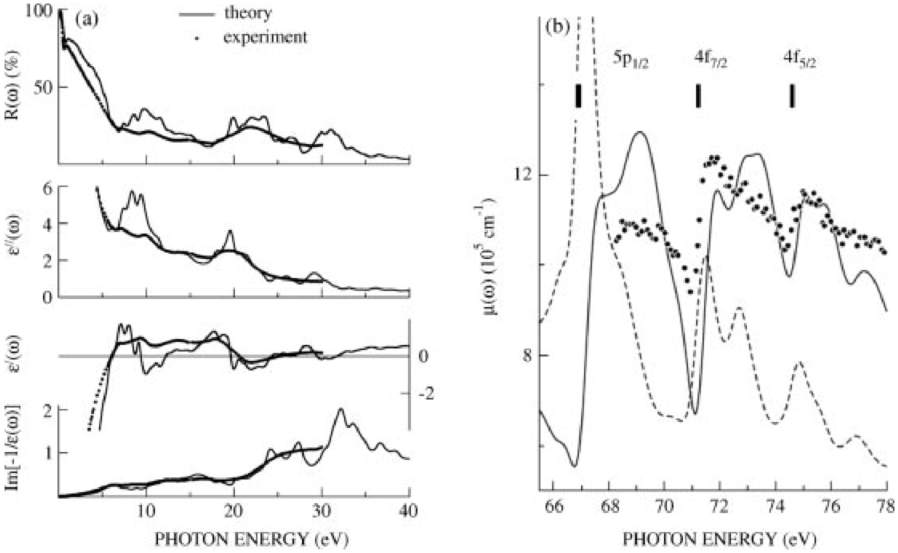

Figure 5.1 (a) The reflectivity $R(\omega)$, the real and imaginary parts of the macroscopic dielectric function $\varepsilon(\omega)$, and the loss function $\mathrm{Im}\left[-\varepsilon(\omega)^{-1}\right]$ of Pt: theory [6] (lines) and experiment [5] (dots). (b) Absorption coefficient $\mu(\omega)$ of Pt: theory with (solid line) and without (dashed line) local fields and experiment [9] (circles). Theoretical energies of 5p and 5f bands are adjusted to XPS measurements (indicated by vertical bars). Reprinted with permission from Ref. [6]. Copyright (2001) by the American Physical Society.

The theory fails at higher energies, however, where absorption is due to highly localized semicore states (see the dashed line in Figure 5.1b). It is shown in Ref. [7] that the problem is caused not only by the errors in quasi-particle energies $E_m(\mathbf{k})$, but also by the simplified form (Eq. (5.1)) of the RPA.

Random phase approximation can be refined by taking into account local field effects [8], that is, by including the short-wavelength response to a long-wavelength perturbation, where $\varepsilon(\omega)$ is $\mathbf{k}$ independent. Thus, one improves the description of electron–electron interaction, while remaining within a one-particle approach. For crystals, the problem is formulated in terms of the microscopic dielectric matrix in the reciprocal space representation $\varepsilon_{\mathbf{GG}'}(\omega)$, whose elements are labeled by the reciprocal lattice vectors $\mathbf{G}$ and $\mathbf{G}'$, each element being a tensor in the real space. The macroscopic dielectric function $\varepsilon(\omega)$ (an element of the tensor) is given by the matrix inverse of the dielectric matrix

$$\varepsilon(\omega) = \frac{1}{\left[\hat{\varepsilon}^{-1}(\omega)\right]_{G=0,G'=0}}, \tag{5.5}$$

$$\begin{aligned}\varepsilon_{\mathbf{GG}'}(\omega) = \delta_{\mathbf{GG}'} - \lim_{q\to 0} \frac{e^2}{4\pi^2|\mathbf{q}+\mathbf{G}||\mathbf{q}+\mathbf{G}'|} \sum_{mn} \int_{\mathrm{BZ}} \mathrm{d}\mathbf{k} \\ \frac{\langle \mathbf{k}+\mathbf{q}n|\mathrm{e}^{i(\mathbf{q}+\mathbf{G}')r}|\mathbf{k}m\rangle\langle \mathbf{k}m|\mathrm{e}^{-i(\mathbf{q}+\mathbf{G})r}|\mathbf{k}+\mathbf{q}n\rangle}{E_n(\mathbf{k}+\mathbf{q}) - E_m(\mathbf{k}) - \hbar\omega + i\hbar\eta},\end{aligned} \tag{5.6}$$

where **q** is the wave vector in the Brillouin zone and η is a broadening parameter. The strong effect of the nondiagonal dielectric response on the far UV optical absorption in Pt is illustrated by Figure 5.1b: the inclusion of microscopic fields is seen to change both the shape and the amplitude of the absorption coefficient $\mu(\omega)$ curve in Figure 5.1b and to shift the absorption bands to higher energies by several eV. The absorption coefficient derived from the true macroscopic dielectric function nearly perfectly agrees with the experiment. Note, however, that in contrast to Figure 5.1a, which was obtained with *ab initio* Kohn–Sham solutions in the local density approximation (LDA) for the valence band of Pt, the one-particle energies of the 5p and 4f bands had to be corrected according to independent X-ray photoemission measurements [6].

Although Kohn–Sham eigenvalues cannot be identified with true quasi-particle energies, experience shows that they are often adequate for delocalized valence bands but are less reliable for core states. Correct quasi-particle equations include many-body effects through a self-energy operator Σ. A state-of-the-art, but still technically challenging approach to Σ in moderately correlated solids is the GW approximation [10]. This approach has been instrumental in calculating the band structure of semiconductors [11], where the LDA is known to strongly underestimate the width of the band gap.

In contrast to metallic systems, in semiconductors the e-h interaction also plays a fundamental role in the formation of optical spectra. It leads to bound excitons and apart from that strongly affects interband transitions. Thus, knowledge of the two-particle Green's function is required. Modern *ab initio* methods treat the problem by solving a Bethe–Salpeter equation (BSE) for the polarization function $\chi_{\mathbf{GG}'}(\mathbf{q},\omega)$ [12]. The macroscopic dielectric function in the limit of small momentum transfer is then given by

$$\varepsilon(\omega) = \lim_{q \to 0} v(\mathbf{q})\chi_{00}(\mathbf{q},\omega). \tag{5.7}$$

The result can be reduced (after certain reasonable simplification) to a formula similar to Eq. (5.1), but with true excitation energies instead of energy differences $E_n(\mathbf{k}) - E_m(\mathbf{k})$ and with a coherent sum over direct e-h pairs instead of the incoherent sum over direct transitions [13, 14]. Thus, apart from obtaining excitation energies within the quasi-particle gap, the two-particle theory also takes into account interference between matrix elements $M^{\mathrm{e}}_{mn}(\mathbf{k})$ coming from different **k** points. The latter effect may affect the interband absorption spectrum much more strongly than the former, in particular for semiconductors. It has been shown that for GaAs [14] and GaN [15] the dramatic shift of the absorption band to lower energies resulting from the e-h interaction is entirely due to a constructive interference of the transition amplitudes at lower energies and destructive interference at higher energies. In wide band gap insulators, the Bethe–Salpeter equation approach reliably describes high-energy excitons. For example, GW–BSE methods have successfully provided a unified description of the optical spectra of rutile and anatase polymorphs of TiO_2, clarifying the role of electronic and optical gaps in materials important for solar energy conversion [16]. Excellent agreement of *ab initio* calculations with experiment has been achieved for a wide range of semiconductors and insulators [13–15, 17] (see also the review article [18] and references therein).

5.2
Band Mapping of Solids by Photoemission Spectroscopy

Photoemission has become a preeminent tool to understand real solids in terms of their electronic structure [19, 20]. In a simplified picture and for sufficiently weak incident radiation, photoemission is a linear process in which one electron is emitted for each photon absorbed. Because the mean free path of photoelectrons ranges typically from a few angstroms to a few tens of angstroms, photoemission measurements are surface sensitive. Depending on the photon energy $\hbar\omega$, the photoemitted electron can be extracted either from atomic-like core levels or from more weakly bound valence levels. In the former case, photoelectron diffraction offers considerable information about structural properties. Identification of the chemical environment is also possible as well from chemical shifts in X-ray photoemission spectra. In the latter case, spectroscopy techniques give rise to valuable information on momentum-resolved band structure: angle-resolved photoelectron spectroscopy (ARPES) is the preferred method for complete band mapping of solids. A schematic drawing of the photoemission process is shown in Figure 5.2.

Although photoemission is actually a many-body process, state-of-the-art theoretical descriptions of the photocurrent I rely on Fermi's Golden Rule in a one-electron picture:

$$I\left(E,\mathbf{k}_{\|}^{0}\right) \propto \sum_{\nu k} \left\langle \psi_f\left(E,\mathbf{k}_{\|}^{0}\right) | \mathbf{O} \middle| \psi_\nu(\mathbf{k}) \right\rangle \delta(E - E_\nu(\mathbf{k}) - \hbar\omega), \tag{5.8}$$

where there is a sum over the continuum of initial states $|\psi_\nu(\mathbf{k})\rangle$ with energy $E_\nu(\mathbf{k})$. The indexes ν and $\mathbf{k}$ refer to the band index and the three-dimensional momentum, respectively. In the one-step photoemission theory, the final state $|\psi_\mathrm{f}\rangle$ is a time-reversed low-energy electron diffraction (LEED) state defined by the surface parallel projection of the Bloch vector $\mathbf{k}_{\|}^{0}$ and energy E. The LEED wave function is a scattering solution for a plane wave incident from vacuum. The LEED state incorporates the effect of the inelastic scattering of the photoelectron, which is quantitatively treated by adding an imaginary part (optical potential) to the potential in the crystal half-space. Therefore, $|\psi_\mathrm{f}\rangle$ is an eigenfunction of a non-Hermitian Hamiltonian with a real eigenvalue E.

The delta function in Eq. (5.8) guarantees total energy conservation. The final state energy E is connected with the measured kinetic energy E_kin by $E_\mathrm{kin} = E - \Phi$, where Φ is the work function of the solid. Momentum conservation is reduced to the parallel momentum $\mathbf{k}_{\|}^{0}$, while the perpendicular component of the momentum is not conserved due to the symmetry breaking by presence of the surface. The operator $\mathbf{O} = \mathbf{A}\cdot\mathbf{p} + \mathbf{p}\cdot\mathbf{A}$ can be written in terms of the vector potential of the photon field $\mathbf{A}$ and the momentum operator $\mathbf{p}$. The $\mathbf{A}\cdot\mathbf{p}$ term describes photon absorption in a homogeneous medium, that is, within bulk of a solid, whereas the $\mathbf{p}\cdot\mathbf{A}$ term has a

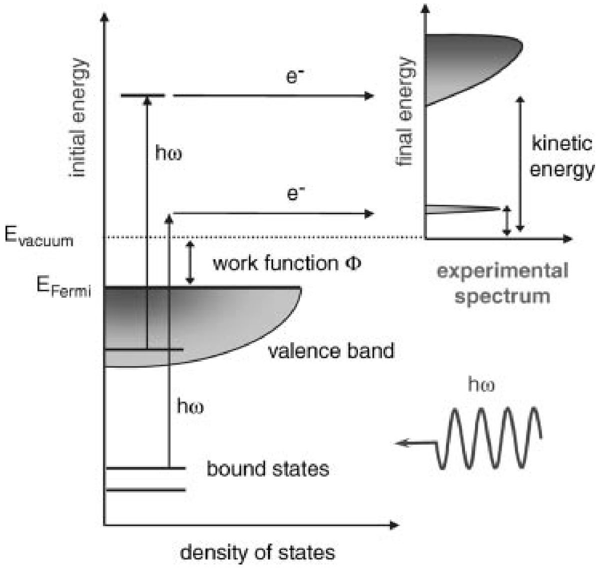

Figure 5.2 Schematic representation of the photoemission process.

significant contribution at a surface, owing to a strong gradient in the vector potential. In the limit of long wavelength and at high photon energy, the vector potential can be approximated as constant (dipole approximation). In metals, below the plasma frequency, this approximation may be unsatisfactory because the exciting field has a strong contribution from the nonlocal dielectric response at the surface, corresponding to the nondiagonal terms in the dielectric matrix of Eq. (5.5). The spatial dependence of the total electric field at the surface, however, can be calculated by modern band structure methods and included into the microscopic theory of photoemission [21].

For ultraviolet (UV) radiation, photoelectrons are extracted from the valence band of the solid. Figure 5.3 shows that an accurate description of the photoemission final state by a time-reversed LEED state $|\psi_f\rangle$ makes it possible to obtain an excellent agreement between theoretical and measured photoelectron spectra for off-normal emission in $TiTe_2$ [22].

The mapping of the solid valence band can be simplified if the final state $|\psi_f\rangle$ in Eq. (5.8) is approximated by a Bloch eigenstate of the bulk system, which conserves the three-dimensional crystal momentum [23, 24]. A further simplification arises if the final state band structure is completely neglected. In this case, and because of the continuum of photoelectron final states, energy conservation is always fulfilled and the matrix elements are constant. Therefore, the sum over initial states in Eq. (5.8) turns into the density of initial states. In this approximation, the spectrum reduces to a one-dimensional density of states (DOS) along the surface normal direction. The example in Figure 5.3, however, shows a crucial role of final-state effects in the

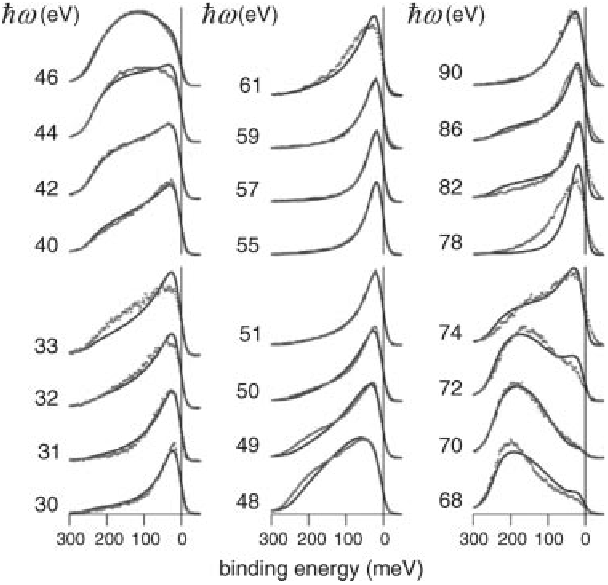

Figure 5.3 Experimental and theoretical energy distribution curves for Ti 3d photoemission in $TiTe_2$. Spectra are marked by photon energies. Reprinted with permission from Ref. [22]. Copyright (2007) by the American Physical Society. (Please find a color version of this figure on the color plates.)

formation of the spectra even for very narrow bands. Their accurate *ab initio* treatment is essential in understanding the photoemission lineshape and its dependence on the photon energy. Modern photoemission theory is capable of taking into account the subtle effects of interference between branches of the complex band structure of the final states and providing a good agreement with the experiment.

Band mapping, such as described in Section 3.4, of occupied states can be considered as a basic application of photoelectron spectroscopy. A more complex task is the derivation of dynamical information from measured lineshapes, linewidths, and peak intensities. Scattering of photoexcited electrons with electrons in the Fermi sea, phonons, and defects, as well as hole screening and decay, can significantly contribute to spectral linewidths [25]. In fact, bulk direct transition linewidths are in most cases dominated by final-state damping. Only in the case of surface states, it is possible to determine the initial state spectral function, without influence of the final state contributions. This feature has been exploited to dissect different contributions from the e-e, e-p, and defect scattering to the linewidths of Shockley surface states of noble metals [26]. Excellent agreement has been obtained between the experimental linewidths and *ab initio* calculations at a level beyond the GW, taking into account the spatial dependence of the screened interaction at a surface [27].

For higher photon energies, electrons can be extracted from core levels for which the theoretical description of the initial electron wave functions is simpler than that for delocalized bands. Spectroscopy in this regime is used for chemical identification, as well as detecting element-specific energy shifts at surfaces. The spatial localization of the initial excitation makes each atom in the solid a point-like source of photoelectrons. Core-level emission is thus a powerful tool for holography and electron diffraction-based techniques [20]. In core-level photoemission, the theoretical description of the photocurrent can be simplified through the three-step model, in which the initial excitation process, the diffraction at the crystal lattice, and the crossing of the surface are considered as three independent processes. Multiple scattering methods have proven to be successful in describing the photoelectron spectra in this regime. The fitting of simulated theoretical spectra to experimental results provides very accurate information on structural parameters of clean and decorated systems, as well as more complex systems [28, 29]. Spin-resolved photoemission provides further insight into the spin structures of surfaces [30–32].

The role of the electron spin is relevant in photoemission processes from magnetic systems, as well as in systems with strong spin-orbit coupling. Spin-dependent phenomena can be investigated through photoelectron spin analysis if the signal levels are sufficient [33]. Even without spin resolution in the photoelectron detection, magnetic dichroism can be used for studying these systems. Magnetic dichroism is based on the change in photoelectron intensity upon reversal of the sample magnetization or the direction of circular polarization of the excitation light [34, 35]. Furthermore, photoemission techniques also provide valuable information on electron correlation. The extreme energy resolution achieved in photoemission measurements in the last years has opened the way to detailed studies of many-body effects in the spectra. This is particularly interesting for the study of strongly correlated systems and superconducting materials, as described in more detail in Chapter 1. Such measurements rely heavily on the ability of photoemission spectroscopy to measure lineshape changes and energy gap shifts with sub-meV resolution [36].

5.2.1
Nonlinear Photoemission as a Band Mapping Tool for Unoccupied States

Nonlinear photoemission processes induced by light sources of high intensity have been shown to be well suited for the study of electronic excitations in solid-state materials. Two-photon photoemission (2PPE) has contributed greatly to the study of ultrafast electron dynamics and adsorbate dynamics at solid surfaces [37, 38]. The lifetime of electronic surface and image states, for instance, has been accurately determined in many systems through pump–probe experiments [39]. In the case of surface states or adsorbate excitations, momentum conservation is relaxed due to the presence of the surface or the localization of the wave functions on the adsorbates [40, 41]. In most cases, 2PPE experiments involve nonresonant excitation or excitations from bulk to surface states that do not involve strong resonance enhancement. This is in part because the excitation lasers have poor tunability, as well as because resonances can complicate interpretation of the spectra.

The spectroscopy of bulk electronic states by 2PPE has not received comparable attention, although it can effectively be used to extend spectroscopy to electronic states below and above the vacuum threshold [42–44]. Other photoemission-based methods, such as inverse photoemission spectroscopy [45, 46], have never attained accuracy comparable to that of ARPES for the occupied states; therefore, establishing a general method with high spectral and temporal resolution for the study of the unoccupied states would be highly desirable. In fact, such methods could have significant advantage for band mapping over conventional ARPES because interband excitations within the bulk of solids rigorously conserve momentum.

In one-photon photoemission, the one-step model (see Eq. (5.8)) is known to provide a firm basis for *ab initio* calculations. A similar approach is expected to be appropriate for the case of multiphoton photoemission. Following perturbation theory, one can show that the second-order contribution to the photoemission current is [47]

$$I \propto \sum_{\nu \mathrm{k}} |h_{\mathrm{f}k}|^2 \delta(E - E_\nu(\mathbf{k}) - \hbar\omega) + \frac{1}{4} \sum_{\nu \mathbf{k}} \left| \sum_{\mu \mathbf{k}'} \frac{h_{\mathrm{f},\mathbf{k}'\mu} h_{\mathbf{k}'\mu,\mathbf{k}\nu}}{E_\mu(\mathbf{k}') - E_\nu(\mathbf{k}) - \hbar\omega - i\eta} \right|^2 \delta(E - E_\nu(\mathbf{k}) - 2\hbar\omega), \tag{5.9}$$

where the first sum corresponds to the first-order process of Eq. (5.8). The second term involves matrix elements between initial and intermediate states $h_{\mathbf{k}'\mu\mathbf{k}\nu}$ and between intermediate and final states $h_{\mathrm{f}\mathbf{k}'\mu}$. The sum over unoccupied intermediate states runs over the band index μ and the three-dimensional momentum $\mathbf{k}'$. The final state $|\psi_\mathrm{f}\rangle$ is again a time-reversed LEED state. In contrast to the relaxed momentum conservation in the transition matrix elements $h_{\mathrm{f}\mathbf{k}'\mu}$ to the inverse LEED state, full three-dimensional momentum is conserved in the intermediate transition $h_{\mathbf{k}'\mu\mathbf{k}\nu}$. This property is crucial to obtain an accurate description of the band dispersion of unoccupied levels. Distinct peaks in the two-photon photoemission yield can therefore be associated with initial to intermediate state resonances that correspond to momentum-conserving transitions. Figure 5.4 illustrates this effect in the case of two-photon transitions in Si(001) [47]. Figure 5.4b shows the photoemission intensity versus the energy (measured with respect to the valence band maximum). In Figure 5.4a, a magnified view of a portion of the band structure that contributes to the photoemission spectrum is shown, and the full band structure is included in the inset as well. Thickened grey lines denote the complex band structure constituents of the LEED states; the thickness gives the contribution of the bulk Bloch wave to the outgoing photoelectron wave function.

Taking full advantage of the band mapping capability of multiphoton photoemission requires broad excitation laser tunability and momentum mapping capability. Owing to the experimental demands, only a few examples of such studies have been reported in the literature [48, 49]. One should also keep in mind that multiphoton excitation processes can occur through multiple resonant and nonresonant pathways, which contribute coherently to the photoemission yield, and therefore one should expect such spectra to be influenced by multiple pathway interference effects. Such multiphoton processes are discussed in Ref. [50].

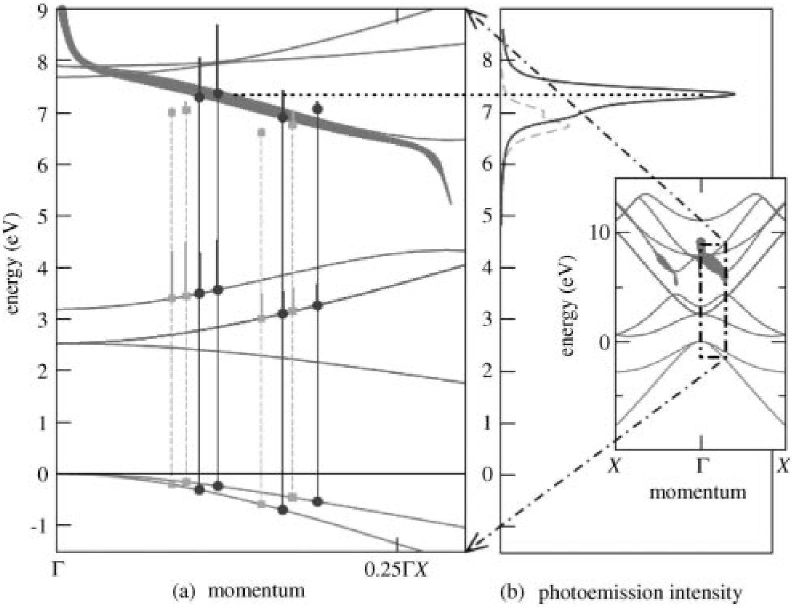

Figure 5.4 Two-photon photoemission yield and some relevant two-photon transitions in Si(001). Right panel: Grey dashed line (dark solid line) corresponds to the spectrum for $\hbar\omega = 3.6$ (3.8) eV. The full band structure is shown in the inset as well. Left panel: A selected part of the band structure is magnified. The transitions relevant for the spectrum are shown by squares (circles) for $\hbar\omega = 3.6$ (3.8) eV. Thicker vertical bars rising from the squares and circles show the magnitude of the coupling matrix elements for the transitions. See text for further explanation. Reprinted with permission from Ref. [47]. Copyright (2008) by the American Physical Society.

5.3
Optical Excitations in Metals

The dielectric function, as described in Eqs. (5.1)–(5.6), is defined by both the electronic structure and carrier phase relaxation phenomena in a solid. Photoemission spectroscopy measures the electronic bands of a solid with energy and momentum resolution. Optical measurements, such as reflectivity and transmission, represent the full electromagnetic response of a solid, which is useful for describing the macroscopic properties, but the nonspecific nature makes it difficult to extract information on the band structure and the specific carrier scattering rates. Nevertheless, optical methods have played an essential role in the development of our understanding of the fundamental properties of metals [51, 52], as well as for ultrafast studies of electron dynamics in solids [53–56]. A valuable theoretical comparison of the spectroscopic and dynamical information content of nonlinear photoemission and optical spectroscopy measurements is given in Ref. [57]. The goal of this section is to analyze the optical response of metals in greater detail in order to describe the processes contributing to different components of the dielectric response and to describe the carrier distributions they generate.

Optical response of a metal involves both single-particle and collective excitations that are described by the complex dielectric function. In the limit of small momentum transfers relevant to the visible/UV spectral response, the complex dielectric function is written as a sum of three terms [8, 51, 58–60]:

$$\varepsilon(\omega) = 1 - \frac{\omega_{p0}^2}{\omega^2 + i\omega/\tau} + \varepsilon^i(\omega), \tag{5.10}$$

where τ represents the electron–hole pair scattering time, to be described in more detail. The first two terms in Eq. (5.10) correspond to the Drude term already introduced in Eqs. (5.2) and (5.3) in the limit of no damping ($\tau \to \infty$). The Drude term describes the intraband single-particle absorption and the plasma excitation. The remaining term corresponds to the Lorentz term given in Eq. (5.1) and describes single-particle interband absorption. Thus, the dielectric function in Eq. (5.10) combines contributions to photon absorption in a metal from electric dipole interband transitions between electronic bands, which conserve energy and momentum and are described by the Lorentz term, with contributions of higher order processes where e-h pair excitation is accompanied by electron, phonon, or impurity/defect (henceforth, just impurity) scattering to conserve overall energy and momentum. All these higher order processes contribute to the Drude term, and their specific contribution is generally difficult to isolate. Photon absorption under ultrafast laser excitation can also occur through multiple photon absorption between bands or through virtual states. The multiphoton excitation process must conserve energy and momentum only for the transition between initial and final states rather than for the individual excitation steps, as already discussed in Sections 3.4 and 5.2.1 [47, 49, 61]. In multiphoton photoemission spectroscopy, the final state is usually the photoemission continuum, where the inverse LEED states automatically satisfy the energy and perpendicular momentum conservation, whereas the parallel momentum remains rigorously that of the initial state (Section 5.2).

Whether interband dipole transitions dominate light absorption depends primarily on the excitation wavelength and the electronic band structure of absorbing material. In metals, there is an energy threshold for interband transitions that corresponds either to **k**-conserving transitions from an occupied band to a point where another partially occupied band crosses the Fermi surface or from Fermi surface crossings to another unoccupied band. Below the interband threshold, light absorption will be determined by a variety of secondary factors, some of which may be under experimental control, such as sample purity, crystallinity, adsorbate coverage, and temperature. The dominant channel for photoabsorption will determine the initial distribution of electrons and holes excited in the sample. This knowledge of the photoexcitation process is often a missing ingredient for describing the primary photoexcited carrier distributions and how they couple to other degrees of freedom, for instance, the unoccupied resonances of surface adsorbed molecules that may undergo hot electron chemistry [62].

5.3.1
Optical Response of Noble Metals

Because of their useful and instructive physical properties, detailed optical, photoemission, and 2PPE studies have been performed on noble metals [44, 51, 52, 63, 64]. As a specific example of photoexcitation in metals, we consider silver, which has well-known and relatively simple optical and electronic properties and its role has been central in developing theories of interaction of electromagnetic fields with solids. Moreover, because of its favorable optical properties, silver features prominently in the field of plasmonics, which will be discussed in Section 5.4. The electronic structure and optical properties of Ag are known from *ab initio* theoretical calculations, and its dynamical response has been examined at the highest level of theory [58, 65–67]. Figure 5.5 shows the calculated electronic band structure of Ag in the high symmetry directions, which defines its complex dielectric function in Figure 5.6 [66]. Even for a relatively simple metal such as silver, the electronic band structures obtained from calculations at the DFT and GW levels show significant deviations from the optical and photoemission measurements [66, 67]. Significant

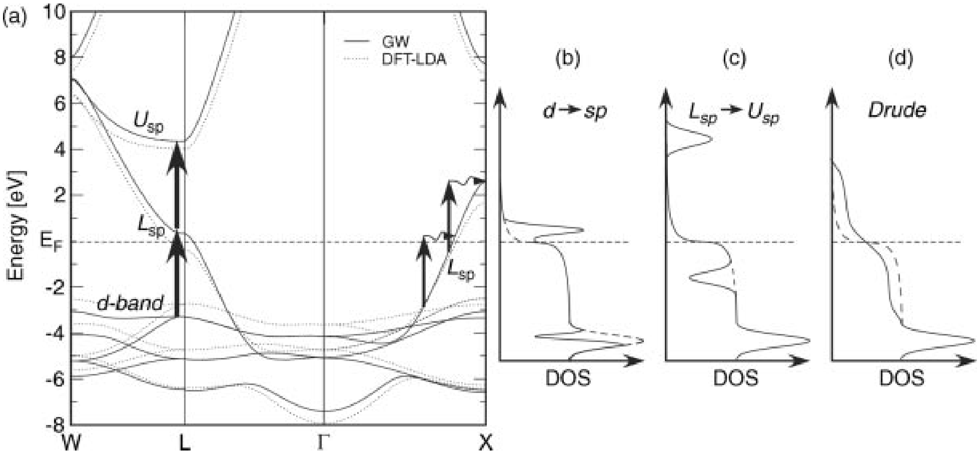

Figure 5.5 (a) The calculated electronic band structure of Ag using the GW and DFT–LDA methods [65, 66] and the possible interband and intraband transitions excited with near-ultraviolet light. The GW calculations place the sp bands at too high energy, whereas the DFT calculations underestimate the binding energy of the d bands. Near the L point, both d $\rightarrow$ sp and $L_{sp} \rightarrow U_{sp}$ transitions are possible. Intraband transitions within L_{sp} occur through a second-order process involving a scattering process necessary to conserve momentum. (b–d) The corresponding modification of the state occupations (DOS × the distribution function) through the interband and the intraband excitation. The dashed lines indicate the initial population before it is modified by absorption of a photon.

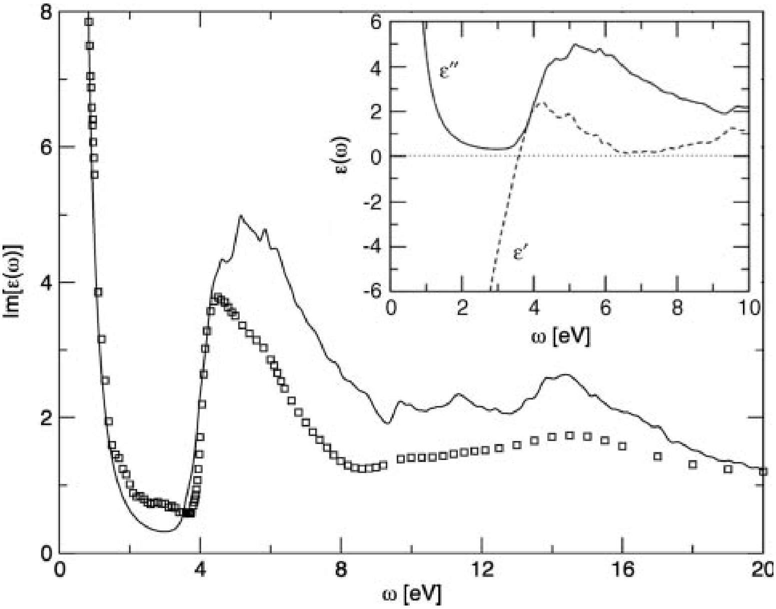

Figure 5.6 The calculated imaginary part of the dielectric constant ε'' of Ag from a GW calculation of Ref. [66] (line). The squares are the experimentally measured values [80]. The inset shows the real and imaginary parts of the dielectric function on the same scale at the onset of the interband excitations, where $\varepsilon' \approx 0$. Inset reprinted with permission from Ref. [66]. Copyright (2002) by the American Physical Society.

improvement between experiment and theory for the optical spectra can be obtained by describing the dynamical excitonic effects through BSE [66]. Even though screening of the Coulomb interaction is efficient in metals, dynamical screening of the interaction between the photoexcited e-h pair is important because of the participation of the d bands with relatively low binding energies in the optical response. Excitonic effects have also been predicted to be increasingly important as the charge density decreases from the bulk value to a few angstroms above a metal surface, where the density-dependent screening response slows down from sub-femtosecond in the bulk to a few femtosecond for image potential (IP) states at surfaces [68].

According to Figure 5.6, the imaginary part of the dielectric constant ε'' of Ag is characterized by the Drude region, which is responsible for decreasing the component that extends from the IR to the near-UV region, and the interband region with a threshold at 3.84 eV. The interband threshold approximately coincides with the crossing of the real part of the dielectric function from negative to positive, that is, $\varepsilon'(\omega) = 0$, which can be seen to occur in Figure 5.6 at 3.92 eV. The $\varepsilon'(\omega) = 0$ condition is responsible for the sharp maximum in the loss function $\mathrm{Im}[-\varepsilon(\omega)^{-1}]$ in Figure 5.7, where the electromagnetic field resonantly drives the collective charge density fluctuations in silver. We describe light absorption in the interband region, and then in the subsequent section in the Drude region.

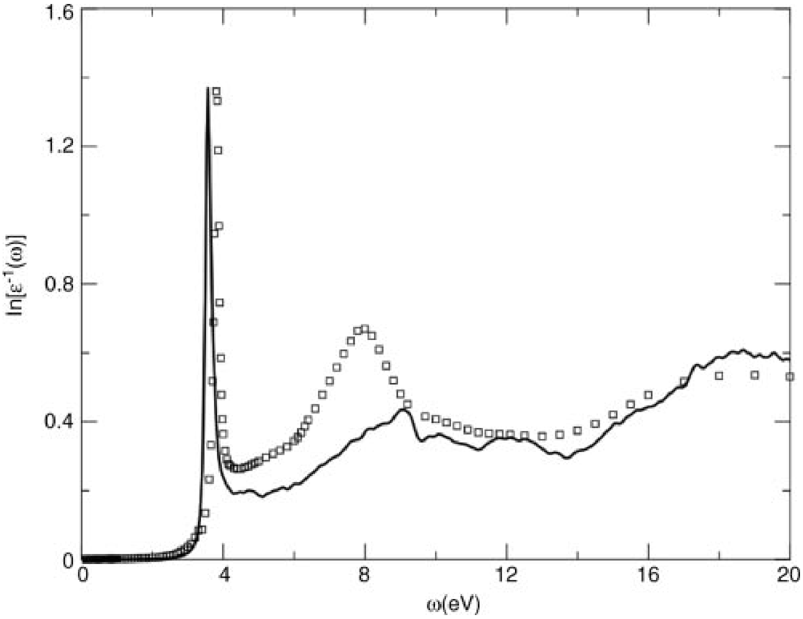

Figure 5.7 The experimental electron energy loss spectrum of silver (boxes) and the calculated (GW) loss spectrum. The major peaks at 3.8 and 7.95 eV are due to the out-of-phase and in-phase screening by sp- and d-band electrons. Reprinted with permission from Ref. [66]. Copyright (2002) by the American Physical Society.

5.3.2
Interband Absorption

At energies below 3.8 eV, direct interband dipole transitions in Ag are not possible according to the band structure in Figure 5.5. Photon absorption by a dipole transition cannot occur, because according to the band structure in Figure 5.5, there are no vertical transitions that couple occupied with unoccupied states. According to the band structure of Ag (Figure 5.5), the onset of interband transitions at 3.84 eV involves two types of excitations [58]. The electronic bands of Ag consist of the partially occupied nearly free electron sp band, which is characterized by a Fermi energy of 5.5 eV (it crosses E_F at several k-space points in high symmetry directions as shown in Figure 5.5). In addition to the sp band, there are fully occupied d bands that extend up to approximately −3.8 eV below E_F. In noble metals, the interband threshold corresponds to momentum-conserving transitions from near the top of the d bands to the sp band at the point where it crosses E_F. Such transitions near the X and L points establish the interband absorption threshold at 3.84 eV [58, 65, 66]. Because the d bands are nearly flat, their contribution to the joint density of states, which are coupled by optical transitions near E_F, is large [63, 69]. In the case of Ag, the threshold region includes an additional resonance at 4.03 eV arising from transition across the L projected band gap from the lower sp band (L_{sp} in Figure 5.5) near its crossing with E_F to the upper sp band (U_{sp} in Figure 5.5) [58, 65, 66]. In the case of copper and gold, the d bands are closer to E_F than for Ag, and therefore their interband thresholds occur at ~2 eV, whereas the $L_{sp} \rightarrow U_{sp}$ excitations across the sp band gap are relatively unchanged from the Ag case.

From the threshold at 3.8 eV, the interband transitions dominate the complex dielectric function of Ag. The band structure in Figure 5.5 portends that in Ag threshold interband photoexcitation generates dominantly energetic holes at the top of d bands near X and L points and electrons near E_F (Figure 5.5b). By contrast, the $L_{sp} \rightarrow U_{sp}$ transition at 4.03 eV generates holes near E_F and electrons at the bottom of U_{sp} (Figure 5.5c). The d band processes dominate the hot carrier generation in noble metals because of their larger joint DOS. Owing to the crystalline symmetry, these interband excitations occur according to Eq. (5.1) along several equivalent lines in BZ that satisfy simultaneously the energy and momentum conservation [63, 69]. Therefore, the initial electron and hole distributions generated by interband excitation are usually strongly localized in energy and momentum according to the specific band structure of the absorbing material and the photon energy, as indicated schematically in Figure 5.5b and c. Such nascent electron distributions can be characterized by angle-resolved two-photon photoemission [43, 61].

Above the interband threshold, the dielectric function exhibits additional structure that reflects the joint DOS in dipole-mediated optical transitions. In particular, features appear at higher energies associated with other critical points that contribute high joint DOS [70]. We also note that for photon energies above the vacuum level (E_{vac}), the conservation of perpendicular momentum is relaxed by the presence of the surface, as noted in Section 5.1.3. The potential discontinuity at the surface allows Bloch states within the bulk to couple to free-electron states in the vacuum without the requirement for conservation of momentum perpendicular to the surface. Under such circumstances, photoemission can occur by separate pathways involving bulk or surface excitations, but starting and terminating at the same initial and final states through interband transitions within the bulk or through surface-mediated processes. Such parallel pathways lead to quantum interference effects that can be diagnosed by their characteristic asymmetric Fano lineshapes in photoemission spectra [44, 71].

The circumstances for interband absorption in transition metals are somewhat different and more complicated than for noble metals [72, 73]. Because both d and sp bands are partially filled for transition metals, in principle, interband transitions could occur with very low photon energies, depending on the separation between the coupled bands at the Fermi surface crossings. Excitation of complex carrier distributions in the phase space is likely, because multiple d bands can participate as the initial and final states. Further complications arise from the spin-orbit splitting of the d bands that are responsible for separate excitation pathways for electrons with the majority and minority spins [74–76]. Excitations to low-lying unoccupied states have been investigated by 2PPE methods for Gd and Ru, among metals, and from d bands to image potential states for Fe and Co [77–79].

5.3.3
Intraband Absorption

In the year 1900, Drude derived a relation $\sigma_0 = (ne^2\tau)/m$ for the DC electrical conductivity of a metal [81]. This is the starting point for the description of the collective electron response responsible for both intraband absorption to be described in this section and the plasmonic phenomena that will follow in Section 5.4. In the Drude model, the electrons in the metal are treated as a freely moving gas with a density n, mass m, and charge e, which can be accelerated during a certain phenomenological relaxation time τ in the direction of an externally applied DC field $\mathbf{E}$ until random scattering processes randomize their momentum. This sequence of acceleration and scattering generates a drift motion of the electrons with velocity $\mathbf{v} = -e\mathbf{E}\tau/m$, which is manifested in the net current density $\mathbf{j} = -ne\mathbf{v} = \sigma_0\mathbf{E}$. Later, Sommerfeld provided a quantum mechanical extension of this model by accounting for the Pauli exclusion principle and the Fermi–Dirac statistics of the electron gas [82]. Corrections to the mass of the conduction electrons due to the finite Coulomb interaction among the electrons and between the electrons and the ionic lattice are often incorporated by replacing m with the effective mass m^*. Within this model, the room temperature DC conductivity of the noble metals gold and silver, which have some of the highest conductivities among metals, is well described by parameters $n_{\mathrm{Au}} = 5.90 \times 10^{-22}\ \mathrm{cm}^{-3}$, $n_{\mathrm{Ag}} = 5.86 \times 10^{-22}\ \mathrm{cm}^{-3}$, $\tau_{\mathrm{Au}} = 30$ fs, and $\tau_{\mathrm{Ag}} = 40$ fs [83]. The effective masses in the conduction bands of Au and Ag are close to unity, $m^*/m_{\mathrm{Au}} = 0.99$, $m^*/m_{\mathrm{Ag}} = 0.96$ [59].

Although the Drude model fails to account for the Fermi–Dirac statistics and Pauli exclusion, it has been remarkably successful in describing the optical response of free electrons in a metal. We will consider in detail the intraband component in the dielectric function within the framework of the extended Drude model (EDM) [84] and its relation to the Lorentz component. Charge carriers in a metal subject to an applied oscillating field are continuously accelerated by the field, but over a cycle of oscillation cannot absorb energy in absence of momentum changing collisions [85]. Such collisions can involve e-e, e-p, or impurity scattering. As Drude absorption requires momentum scattering, the electron distributions excited are not localized in k-space and mainly depend on the photon energy, as well as total density of the occupied and unoccupied states that conserve energy and momentum through a secondary momentum scattering process. The degree to which electron scattering is isotropic depends on the material and the scattering process [85]. On the one hand, if a quasielastic scattering process mediates the optical transition, the energy distribution excited within a solid will be determined primarily by the photon energy. Drude absorption will excite hole states between $E_{\mathrm{F}}-\hbar\omega$ to E_{F} and electron states from E_{F} to $E_{\mathrm{F}} + \hbar\omega$. If the occupied and unoccupied DOS vary slowly in the optically coupled region, as can be expected when sp bands cross E_{F}, the energy distribution should resemble that shown in Figure 5.5d. Because sp bands deviate from the free-electron dispersion most strongly near the Brillouin zone boundaries, the Drude distributions could be quite anisotropic in k-space [86]. Isotropic distributions in

k-space corresponding to a DOS that is constant in energy are often assumed by default in photoexcitation of metals, but such distributions can be justified only for free-electron metals, such as alkali metals, when the Drude absorption is the dominant excitation channel. To observe the nascent electron distributions from Drude absorption, however, would require laser pulses with durations that are shorter than the electron scattering times (typically ~20 fs for electrons at the Fermi level for noble metals). More typically, pulses of 50–100 fs duration are employed, so the observed photoelectron distributions in 2PPE experiments, for instance, are found to follow a Fermi–Dirac distribution described by a rapidly evolving temperature that decreases with pump–probe delay on account of electron–electron (e-e) and electron–phonon (e-p) scattering [77, 78, 87]. If, on the other hand, momentum conservation in an optical transition is achieved through e-e scattering, the photon energy is distributed between at least two electrons and two holes that conserve overall energy and momentum. Therefore, the hot electron distribution will already partially relax in the process of photon absorption through the first cycle in an e-e scattering cascade. Such Auger-like processes could be particularly efficient for intraband absorption above the interband threshold of metals and have been described in case of copper in Figure 2.32 [88, 89].

To describe intraband absorption, Eq. (5.10) for the complex dielectric function includes a phenomenological damping term. The dielectric function can equivalently be expressed in terms of complex optical conductivity

$$\varepsilon(\omega) = \varepsilon'(\omega) + i\varepsilon''(\omega) = \varepsilon_\infty + \frac{4\pi i \sigma(\omega)}{\omega}. \tag{5.11}$$

In Eq. (5.11), $\varepsilon_\infty = 1 + 4\pi N \alpha$ is the effective dielectric constant with the second term describing the core polarization in terms of the ionic polarizability α and the number density N. The core polarization includes the renormalization of the low-frequency response by the high-frequency interband excitations. In the case of noble metals, this term is dominated by the d- to sp-band excitations, that is, the interband contribution of the Lorentz term. As for Eqs. (5.2) and (5.3), the real and imaginary parts of the dielectric constant are related by causality; that is, they are constrained by the Kramers–Kronig relationship [65, 90].

For a free-electron gas (FEG), the intraband optical conductivity of a metal is given in terms of the Drude parameters, that is, the free-electron plasma frequency, ω_{p0}, and the phenomenological damping constant, τ:

$$\sigma(\omega) = \frac{\omega_{p0}^2}{4\pi(\tau^{-1} - i\omega)}. \tag{5.12}$$

Treating Ag as an FEG with n given by the density of 5s electrons of 5.85×10^{22} cm^{-3} predicts a plasma frequency of 8.98 eV [65]. The actual plasma frequency should be different because of electron–electron interactions and screening by the interband excitations.

Alternatively, the plasma frequency can be obtained by using the sum rule for the real part of the conductivity [90]:

$$\int_0^\infty \sigma'(\omega)\,\mathrm{d}\omega = \frac{\omega_{\mathrm{p0}}^2}{8}. \tag{5.13}$$

In practice, σ' is known only in a finite frequency range and has to be extrapolated to frequency regions where measurements are not available. Another estimation of ω_{p0} is available from the high-frequency limit of the real part of the dielectric constant,

$$\varepsilon'(\omega) \approx \varepsilon_\infty - \frac{\omega_{\mathrm{p0}}^2}{\omega^2}, \tag{5.14}$$

under the assumption that $\omega\tau \gg 1$. The same approximation gives the relaxation time from the imaginary part of the dielectric constant as

$$\varepsilon''(\omega) \approx \frac{\omega_{\mathrm{p0}}^2}{\omega^3\tau}. \tag{5.15}$$

For noble metals in the IR/visible spectral range, the assumption that $\omega\tau \gg 1$ holds true [52, 84].

Whereas the plasma frequency has a clear interpretation, the scattering time has contributions from many possible momentum scattering processes. These processes can be extrinsic, involving impurity scattering, or intrinsic, involving e-e, e-p, or other quasi-particle scattering [91–94]. Within the Fermi liquid theory, it is well established that e-e scattering rate has a quadratic dependence on the electron energy [95–97]. Therefore, one expects the scattering time to be frequency dependent. The characteristic frequency dependence of $\tau(\omega)$ is often used as a diagnostic of the material-dependent dominant scattering processes contributing to the Drude absorption, as discussed further in Section 5.3.5 [52, 93, 94].

5.3.4
Extended Drude Model

Causality demands that if $\tau(\omega)$ is frequency dependent, so is the plasma frequency $\omega_{\mathrm{p}}(\omega)$ [65, 84]. The consequences of the frequency dependence of $\tau(\omega)$ are described within the extended Drude model. First, we will develop the EDM and then discuss some origins of the frequency-dependent scattering rate.

In EDM, we derive $\tau(\omega)$ and the frequency-dependent plasma frequency, $\omega_{\mathrm{p}}(\omega)$, from the complex optical conductivity, constraints imposed by the sum rule of Eq. (5.13), and causality. The components of optical conductivity can be obtained from Eq. (5.12) in terms of the frequency-dependent $\tau(\omega)$ and $\omega_{\mathrm{p}}(\omega)$:

$$\sigma'(\omega) = \frac{\omega_{\mathrm{p}}^2\tau^{-1}}{4\pi(\tau^{-2}+\omega^2)}, \qquad \sigma''(\omega) = \frac{\omega_{\mathrm{p}}^2\omega}{4\pi(\tau^{-2}+\omega^2)}. \tag{5.16}$$

The expressions in Eq. (5.16) satisfy causality, which requires that $\sigma'(-\omega) = \sigma'(\omega)$ and $\sigma''(-\omega) = -\sigma''(\omega)$ are even and odd functions of ω. They can be solved for $\tau(\omega)$

and $\omega_p(\omega)$. The relaxation time is obtained from the ratio of the real and the imaginary conductivity

$$\frac{1}{\tau(\omega)} = \frac{\omega\sigma'(\omega)}{\sigma''(\omega)}. \tag{5.17}$$

Taking the real and imaginary parts of Eq. (5.12) gives another pair of equations,

$$\frac{1}{\omega_p(\omega)^2} = \frac{1}{4\pi\omega}\mathrm{Im}\left(\frac{-1}{\sigma(\omega)}\right), \qquad \frac{1}{\tau(\omega)} = \frac{\omega_p(\omega)^2}{4\pi}\mathrm{Re}\left(\frac{1}{\sigma(\omega)}\right), \tag{5.18}$$

which together with Eq. (5.17) yield a set of equations that give $\tau(\omega)$ and $\omega_p(\omega)$ even if the frequency dependence of $\omega_p(\omega)$ is unknown [84].

When considering a Fermi liquid, as described in Chapter 2, rather than a free-electron gas, the quasi-particle mass and therefore $\tau(\omega)$ and $\omega_p(\omega)$ are renormalized through e-e interaction. The renormalization can be expressed through a mass enhancement factor λ, such that $\lambda = m^*/m^{-1}$. Then the renormalized quantities become

$$\omega_p(\omega) = \frac{\omega_{p0}^2}{1+\lambda(\omega)}, \qquad \tau(\omega) = (1+\lambda(\omega))\tau_0(\omega), \tag{5.19}$$

where $\tau_0(\omega)$ is the free-electron scattering time. With ω_{p0} calculated from the carrier density, Eq. (5.19) can be substituted into Eq. (5.18) to obtain $\lambda(\omega)$ and $\tau_0(\omega)$

$$1+\lambda(\omega) = \frac{\omega_{p0}^2}{4\pi\omega}\mathrm{Im}\left(\frac{-1}{\sigma(\omega)}\right), \qquad \frac{1}{\tau_0(\omega)} = \frac{\omega_{p0}^2}{4\pi}\mathrm{Re}\left(\frac{1}{\sigma(\omega)}\right). \tag{5.20}$$

From the symmetry properties of the real and the imaginary optical conductivity, it is evident that $\lambda(\omega)$, $\tau_0(\omega)$, $\omega_p(\omega)$, and $\tau(\omega)$ are even functions of ω.

We can now compare the Drude parameters from EDM with the experimental loss function of Ag in Figure 5.7. The loss function shows a broad peak with high spectral weight at 8.0 eV, which is to be compared with the renormalized plasmon frequency of 9.2 eV (here the renormalization factor from EDM is $1+\lambda(\omega) = 0.95$) calculated from the conduction band electron density [65]. In addition to the experimentally observed plasmon at 8.0 eV, we already noted the prominent sharp peak that occurs when $\varepsilon'(\omega) = 0$ with a smaller spectral weight at 3.9 eV [66]. This peak is too far removed from the renormalized plasmon frequency to be attributed exclusively to the response of the conduction electrons. Its origin can be rationalized by noting that plasmonic excitations occur when $\varepsilon(\Omega) = 0$, where Ω is complex-valued frequency with a small imaginary part, and for $q = 0$. Neglecting the damping effects, the dielectric function can be written as

$$\varepsilon(\omega) = \varepsilon_\infty - \frac{\omega_p^2}{\omega^2}. \tag{5.21}$$

The solution for $\varepsilon(\Omega) = 0$ occurs for $\omega_p^* = \omega_{p0}/\sqrt{\varepsilon_\infty}$ eV, which we understand as the plasma mode of sp band electrons dressed by a virtual cloud of interband excitations of d and sp bands. Thus, in Ag, as in other noble metals, the free-electron plasma peak occurs within a continuum of interband excitations, leading to its significant broadening and renormalization (see Figure 5.7). Because in Ag the $\varepsilon(\Omega) = 0$ condition occurs right below the interband threshold, where the imaginary part of Ω is small, the loss spectrum also has a sharp component associated with the plasma response renormalized by the interband excitations [65]. Thus, two peaks in the energy loss spectrum of Figure 5.7 at 7.95 and 3.9 eV can be considered as the collective oscillations of the sp- and d-band electrons, where the two components oscillate in phase for the former and out of phase for the latter [58, 65, 98]. In Cu and Au, the $\varepsilon(\Omega) = 0$ condition occurs within the interband excitation continuum, and therefore a sharp out-of-phase peak is not observed. Nevertheless, the plasmonic responses of Ag and Au, to be described in Section 5.4, arise from the out-of-phase responses of the sp- and d-band electrons of these metals.

5.3.5
Frequency-Dependent Scattering Rate

By applying EDM to the experimentally measured complex, frequency-dependent dielectric function of a metal, we can derive several useful dynamical properties, such as the frequency-dependent plasma frequency and scattering time, and the renormalization of the free-carrier response by the interband excitations. Perhaps the most interesting and difficult quantity to calculate is $\tau(\omega)$, which we discuss in more detail.

A plot of $\tau^{-1}(\omega)$ versus ω^2 obtained by plotting Eqs. (5.17) or (5.18) can often be used as a diagnostic for the quasi-particle interactions in simple and correlated metals [52, 84, 85, 91–94, 99–102]. In Figure 5.8, we show such a plot for Cu, Ag, and Au. The frequency dependence of $\tau^{-1}(\omega)$ can be assumed to have the general form given by [52, 92]

$$\tau^{-1}(\omega) = \tau_0^{-1}(T) + a(T)\omega + b(T)\omega^2. \tag{5.22}$$

The form of Eq. (5.22) is expected to be valid in a frequency band above the low-frequency region, which is dominated by electron–boson (e.g., phonon) coupling, and below the interband threshold. Outside these limits, $\tau^{-1}(\omega)$ is strongly material dependent, whereas in the intermediate region, it is expected to follow the simple frequency and temperature dependence of Eq. (5.22). The exact behavior depends on the dominant mechanism for momentum scattering of e-h pairs coupled by the optical transition. The frequency dependence of $\tau^{-1}(\omega)$ has therefore been used to analyze the scattering processes that define the optical conductivity in metals, as well as the optical and transport properties in strongly correlated materials [52, 91–93, 101, 102].

In addition to Eq. (5.22), we also assume the validity of Matthiessen's rule, which allows us to write the total scattering rate as a sum of independent contributions from e-e, e-p, surface, and impurity scattering,

$$\frac{1}{\tau(\omega, T)} = \frac{1}{\tau_{\text{e-e}}(\omega, T)} + \frac{1}{\tau_{\text{e-p}}(\omega, T)} + \frac{1}{\tau_s} + \frac{1}{t_i}. \tag{5.23}$$

The last two terms in Eq. (5.23) arise from the breakdown of the translational invariance of a crystal in the presence of a surface $\left(\tau_{\mathrm{s}}^{-1}\right)$ or impurities $\left(\tau_{\mathrm{i}}^{-1}\right)$. We

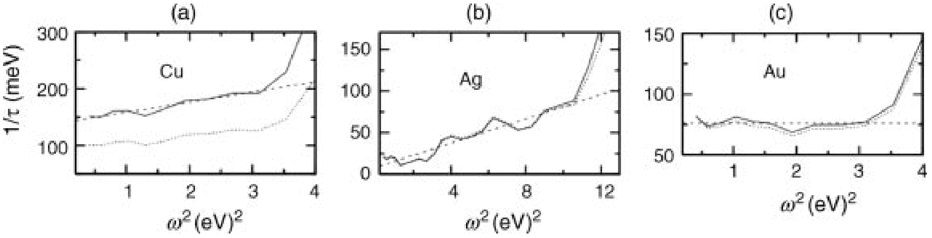

Figure 5.8 Plot of the dependence of $\tau^{-1}(\omega)$ on ω^2 for (a) Cu, (b) Ag, and (c) Au below the interband excitation threshold. The ω^2 dependence is found for Cu and Ag but not Au. Reprinted with permission from Ref. [85]. Copyright (2007) John Wiley and Sons.

assume that both these processes are independent of ω and T [52, 100], and therefore, contribute only to the intercept of a plot of τ^{-1} versus ω or T.

The surface contribution depends on the optical skin depth. As required by momentum conservation, surface absorption will have significant contribution only if $qv_F > \omega$, where q is a scattering wave vector. If the skin depth δ is larger than the distance v_F/ω traveled by an electron during the period of the radiation field oscillation, the surface absorption will be negligible [99]. The surface absorption should be significant only at low frequencies and low temperatures, but the frequency range falls outside the range of validity in Eq. (5.22).

The contribution of e-p scattering can be estimated through a FEG approach [99]. The FEG scattering rate depends on the probability of the second-order process involving simultaneous absorption of a photon and absorption or emission of a phonon to satisfy energy and momentum conservation of the overall process. Therefore, the Debye frequency and temperature will determine ω and T range where τ_{ep}^{-1} has a significant variation. The phonon contribution to Drude absorption according to FEG is

$$\frac{1}{\tau_{\text{ep}}(\omega, T)} = \frac{2\pi}{\omega}\int_0^{\omega} d\Omega(\omega-\Omega)\alpha_{\text{tr}}^2 F(\Omega). \tag{5.24}$$

Here, Ω is the phonon frequency and $\alpha_{\text{tr}}^2 F(\Omega)$ is the phonon DOS weighted by the amplitude for large-angle scattering on the Fermi surface (see Section 2.2.3). Umklapp processes can be included explicitly in the calculation of $\alpha_{\text{tr}}^2 F(\Omega)$. The scattering time is frequency dependent in the region spanned by the phonon spectrum. The phonon contribution to the scattering time goes to infinity as ω^{-5} for frequencies below the Debye frequency, similar to the phonon scattering contribution to electrical conductivity. The low-frequency behavior of the Drude scattering time, $\tau^{-1}(\omega)$, is useful in studies of superconductivity because it provides information on e-p interaction strength through $\alpha_{\text{tr}}^2 F(\Omega)$ and on the superconducting gap 2Δ. For a superconducting system, the upper limit of integration in Eq. (5.24) is changed to $\omega - 2\Delta$ and the frequency dependence of τ_{ep}^{-1} reflects the corresponding changes in the integral of Eq. (5.24) [99].

The conventional e-p contribution to $\tau^{-1}(\omega)$ appears only in the temperature-dependent intercept $\tau_0^{-1}(T)$ because Eq. (5.22) is valid only above the Debye frequency. The surface and defect scattering contributions can be distinguished as a temperature-independent offset of $\tau_0^{-1}(T)$ from the extrapolated $T = 0$ value of the $\tau_{\mathrm{ep}}^{-1}(T)$.

Numerous studies of the optical properties of the relatively simple noble metals have been used to validate the Drude theory. In the frequency range from 0.6 eV up to the interband absorption onset, the frequency dependence of Eq. (5.22) is dominated by the $b\omega^2$ term for Cu and Ag, as can be seen in Figure 5.8. Whether this ω^2 dependence arises from e-p or e-e scattering, however, is controversial and uncertain [52, 84, 91, 92, 103, 104]. By extending the Fermi liquid theory to describe the e-e scattering contribution to optical conductivity [105, 106], Christy and coworkers proposed that the e-e scattering should lead to a scattering rate of the form

$$\tau_{\mathrm{ee}}^{-1}(\omega, T) = b\omega^2 + c(k_{\mathrm{B}}T^2). \tag{5.25}$$

As in the case of electrical conductivity, the temperature dependence of Eq. (5.25) should be observed only at sufficiently low temperatures where the e-p contribution is frozen out [106]. This term makes a contribution to the intercept of Eq. (5.22), which is too small to identify considering the uncertainties in performing and evaluating the optical measurements. The $b\omega^2$ term is a consequence of the energy dependence of the phase space for e-e scattering in a three-dimensional Fermi liquid [96]. The e-e scattering time according to the Fermi liquid theory is given by

$$\tau_{\mathrm{ee}}(E) = 263 r_{\mathrm{s}}^{-5/2}(E - E_{\mathrm{F}})^{-2}\,\mathrm{fs\,eV}^2, \tag{5.26}$$

where r_{s} is the electron density parameter (see also Section 2.4.3.2) [97, 107]. Equation (5.26) gives the e-e scattering time for an electron at a specific energy above E_{F}, whereas the frequency dependence of Eq. (5.25) arises from the scattering of an e-h pair coupled by photons of energy $\hbar\omega$. Therefore, the optical scattering rate with the $b\omega^2$ dependence is an average of the scattering rates of holes in the energy range from $E_{\mathrm{F}} - \hbar\omega$ to E_{F} and electrons from E_{F} to $E_{\mathrm{F}} + \hbar\omega$ [52].

Although it is quite reasonable that above the Debye frequency the Drude scattering rate of noble metals should be dominated by e-e scattering, the measured parameter b is several times too large in comparison to the e-e scattering rates deduced from transport measurements. In order to explain this discrepancy, Smith, Cisneros, and coworkers pointed out that the Umklapp contribution of e-p scattering should also follow the quadratic dependence in frequency and therefore contribute to the $b\omega^2$ term [52, 104]. The e-p mechanism, however, predicts b to be temperature dependent, but this is not found in the temperature-dependent measurements of $\tau^{-1}(\omega, T)$ for Cu, Ag, and Au [92].

The interpretation of the frequency and temperature dependence of $\tau^{-1}(\omega, T)$ for noble metals is thus still not fully understood, yet Drude theory is actively being applied as a diagnostic for electron scattering processes in, for instance, strongly correlated materials. For example, in high-temperature superconductors, where the $a\omega$ term in Eq. (5.22) often dominates, the linear dependence has been examined in terms of the bosonic interactions that give rise to exotic superconductivity and the marginal Fermi liquid behavior [93, 94, 101]. The applications of EDTand particularly the frequency dependence of the scattering rate on highly correlated materials are discussed at length in the review by Basov and Timusk [93].

5.3.6
Surface Absorption

So far we have considered only the role of bulk dielectric properties of metals in the absorption of light. The effect of the surface appeared only as a source of momentum due to the finite optical skin depth. A surface can also influence absorption on account of the intrinsic or adsorbate-induced electronic structure with implicit relaxation momentum conservation on account of reduced dimensionality and disorder.

Surface absorption is well documented under UHV conditions where surface science methods are used to prepare atomically ordered samples. Perhaps the most detailed studies have been performed on the anisotropic absorption at (110) surfaces of noble metals [108–112]. The anisotropy of the surface makes it possible to separate the surface contribution from the isotropic bulk response. For example, the reflectivity of a Cu(110) surface has a sharp drop at 2.0 eV, attributed to a transition between an occupied Shockley surface state at −0.4 eV to an unoccupied surface state at 1.6 eV (Figure 5.9). This surface is peculiar in having two low-energy surface states within the $\bar{Y}$ projected band gap. These surface states are relatively sharp because their wave function penetration into the bulk is small, and, therefore, the inelastic scattering of the surface state electrons and holes with the bulk carriers is constrained. Moreover, the surface states have similar dispersions, leading to a large joint DOS for optical transitions. Both these factors contribute to a sharp absorption feature that is observed in the anisotropic reflectivity spectrum. This resonance is sensitive to the adsorption of impurities at low coverages because the extremely efficient scattering of surface state electrons leads to the resonance broadening [110, 113]. When adsorbates form highly ordered layers, however, such as the oxygen-induced (2×1) reconstruction of a Cu(110) surface, adsorbate-localized excitations can also contribute to sharp spectroscopic features in surface reflection spectra [109, 111].

In addition to surface localized interband transitions, a complete description of light absorption at surfaces should also include the surface-to-bulk and bulk-to-surface optical transitions. Such transitions are known to happen from two-photon photoemission spectroscopy. For instance, studies of coherent control of photoinduced current involving the $n = 1$ image potential state of a Cu(001) surface rely on the coherent excitation from the occupied bulk sp band near E_F [114]. Although such processes can happen with high efficiency, as evidenced by the intense IP state signal from Cu(001), the coupling of 3D bulk with 2D surface bands is unlikely to contribute distinct features in the optical spectra because such transitions have relatively low joint DOS and they occur above the interband threshold for bulk excitations. In the case of Cu(001), the threshold for IP state excitation at ~4.0 eV overlaps with the more intense d- to sp-band interband spectrum. Transitions between bulk and surface

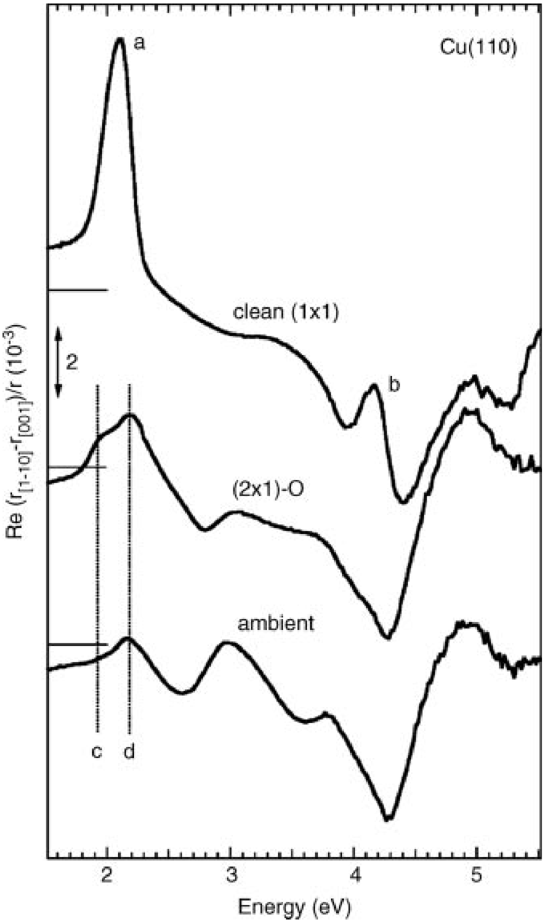

Figure 5.9 Plot of the anisotropic reflectivity from Cu(110) and Cu(110)-(2 × 1)-O surfaces in ultrahigh vacuum and air. Peaks a–d involve transitions between surface states. Reprinted with permission from Ref. [110]. Copyright (2000) by the American Physical Society.

bands might have more significant contributions to the dielectric function below the interband threshold. For instance, the onset of excitations from the sp band to an unoccupied part of the Shockley surface state should have an onset above ~0.3 eV for Ag(111) and Cu(111) surfaces [115, 116]. Such transitions have recently been found in 3PPE spectra of Cu(111) [117].

Finally, we turn our attention to isolated adsorbates on metal surfaces. UHV surface studies have shown that adsorbates can have significant effect on the dielectric functions of metals through resonant or nonresonant effects [110, 118, 119]. Surface adsorbates are impurity scattering centers, similar to bulk defects, and therefore can enhance intraband absorption by acting as other nonresonant sources of momentum. Electronic states of impurity atoms and molecules can also act as resonant absorbers of electromagnetic energy. This is most clearly seen in two-photon photoemission spectra of alkali atoms on noble metal surfaces, where resonant excitation from substrate to adsorbate-localized states is evident in optical dephasing of coherent two-photon absorption [120–123]. Although there are many examples in the literature claiming hot electron excitation of adsorbates on metals, where presumably electron–hole pairs are absorbed by metal and hot electrons scattered into adsorbate resonances [124, 125], most experimental studies of adsorbate resonance-mediated two-photon photoemission are consistent with the direct excitation from bulk bands of the substrate to adsorbate-localized resonances [126]. Because excitation occurs to localized states, such charge transfer processes need to conserve only energy. The transition probability depends on the optical transition moment and the overlap between the Bloch waves of the substrate and localized resonance wave functions of adsorbate. Unfortunately, such interfacial charge transfer excitation processes have yet to be described by theory.

5.3.7
Summary

In this section, our goal was to describe photon absorption processes at metal surfaces. Traditionally, the optical response of metals has been understood on the basis of the complex dielectric function. The dielectric function incorporates the electronic band structure and the dynamical many-body response of a system to an external electromagnetic perturbation. Far more detailed information on the material response available to linear optical methods such as ellipsometric measurements can now be obtained by means of nonlinear optical spectroscopy and, in particular, by angle, energy, spin, and time-resolved photoemission [43, 49, 76, 112, 114, 127]. Such measurements can be typically understood from the static band structure of metals, but experiments and theory are advancing to the attosecond timescales, where effects of the coherent many-body response of metals should have measurable effects [68, 128, 129]. We believe that further progress in the understanding of the optical response of metals can be made by quantitative time-resolved two-photon photoemission measurements in partnership with electronic structure theory.

5.4
Plasmonic Excitations at Surfaces and Nanostructures

In the previous section, we described the optical excitation processes in metals. The focus has been primarily on single-particle excitations, though we found that the collective response associated with the plasma excitations plays an important role in defining the dielectric properties of metals. This section describes the collective plasma response, particularly in how it affects the optical properties of metallic particles with different geometries and in different dielectric environments. Specifically, effects of the shape of metallic nanostructures on their linear optical properties will be addressed. Starting with very simple geometries, the fundamental optical excitations of extended interfaces (surface plasmon polaritons [130]) and of nanoparticles (localized surface plasmons [131, 132]) will be introduced. Structures with novel and interesting optical functionality can be designed by fabricating nanostructures supporting both propagating and localized surface plasmon polariton fields and will be discussed for specific examples of subwavelength gratings and adiabatic metallic tapers. Finally, some recent ideas for coupling surface plasmon fields to excitonic excitations in hybrid metal/dielectric nanostructures will be presented. Much of the discussion will focus on optical properties in the visible and near-infrared range, treating the local dielectric function of the metal in terms of the Drude model introduced earlier in this chapter.

5.4.1
Drude Model for Optical Conductivity

When applying a harmonic time-varying electric field $\vec{E}(t) = \vec{E}_0\,\mathrm{e}^{-i\omega t}$ of frequency ω, collective oscillations of the free-electron gas are induced. Their amplitude $\vec{x}(t)$ is given by the equation of motion $m(\ddot{\vec{x}} + (\dot{\vec{x}}/\tau)) = -e\cdot\vec{E}$, inducing a dipole moment per electron of $\vec{p}(\omega) = -e\vec{x}(\omega) = (e^2/m)(1/(\omega^2 + (i\omega/\tau))$ and hence a macroscopic polarization $\vec{P} = ne\vec{x} = (\varepsilon - 1)\varepsilon_0\vec{E}$. In this approach, the frequency-dependent dielectric function $\varepsilon(\omega)$ is thus given by the intraband contribution to Eq. (5.10) [133, 134]. Using Ohm's law, $\vec{j}(\omega) = ne\dot{\vec{x}}(\omega) = \sigma(\omega)\vec{E}(\omega)$, gives the relationship between the external field and the induced current density in terms of optical conductivity, as given in Eq. (5.12). Therefore, the collective response of the electron plasma in the metal results in a dielectric function with a large negative real part and a much smaller positive imaginary part in the infrared and visible spectral ranges, as described in Section 5.3. In the high-frequency limit, ε approaches unity.

Experimental values for the dielectric function of gold and silver up to the interband thresholds, taken from Ref. [60], are shown in Figure 5.10, together with a fit to Eq. (5.10), ignoring $\varepsilon_i(\omega)$ and assuming plasma frequencies of $\omega_{\mathrm{p,Au}} = 9.1$ eV and $\omega_{\mathrm{p,Ag}} = 9.2$ eV, respectively. The existence of the plasma response at these frequencies is evident from the dielectric and loss functions of Ag in Figures 5.6 and 5.7, which extend into the higher energy range than Figure 5.10. The phenomenological damping times, taken to be frequency independent, are $\tau_{\mathrm{Au}} = 9.3$ fs and $\tau_{\mathrm{Ag}} = 31$ fs, respectively. It is evident that the dielectric functions of silver and gold essentially follow the predictions of the Drude model for energies up to their interband thresholds at about 3.8 and 2.0 eV if values $\varepsilon_{\infty,\mathrm{Ag}} = 4.0$ and $\varepsilon_{\infty,\mathrm{Au}} = 7$ are assumed. In Figure 5.10 (solid lines), the interband contribution to the dielectric function $\varepsilon_i(\omega)$ is modeled phenomenologically as a sum over transitions at critical points in the joint density of states that are coupled by optical excitation as described in Eq. (5.1) [135]. For gold, a reasonable agreement with the experiment is reached by including two transitions, $i = 1, 2$, whereas for silver more resonances are needed [135, 136]. Effects connected with a nonlocal (**k**-dependent) response of the metal [137, 138], relevant for particle sizes of less than 10 nm, will not be considered here. It is currently believed that such a local Drude-like dielectric function can

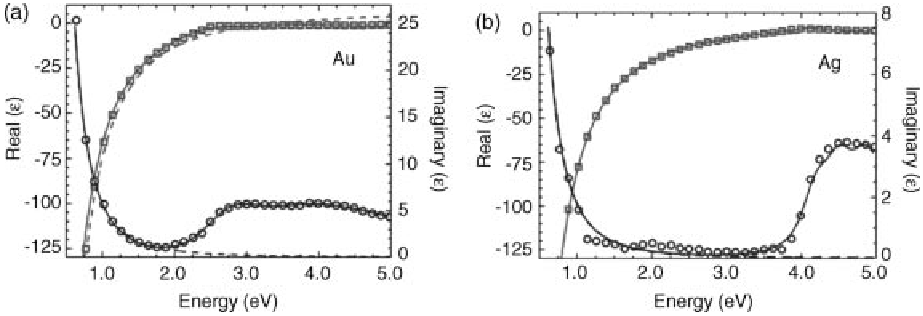

Figure 5.10 The real and imaginary parts of the dielectric function of (a) gold and (b) silver. The experimental data (open circles) are taken from Ref. [60]. The dashed lines indicate fits to the Drude model (Eq. (5.10)) without the interband term $\varepsilon_i(\omega)$. The solid lines represent fits to the Drude model, including a phenomenological description of $\varepsilon_i(\omega)$.

account for the majority of collective optical phenomena at metal surfaces [139–142]. More refined description of the optical response of noble metals can be obtained by EDM, as described in Section 5.3.1.

5.4.2
Interaction of Light with a Planar Metallic Surface

In combination with Maxwell's equations, the dielectric function of metals as represented by the Drude model directly accounts for the mirror-like reflectivity at frequencies below the plasma frequency. We consider a planar interface, located at $z = 0$, between a semi-infinite and nonmagnetic metal with a local dielectric function $\varepsilon_1(\omega)$ and a dielectric with $\varepsilon_2(\omega)$. The metal lies in the negative half-space, $z < 0$. The corresponding complex refractive indices $n_i = n'_i + in''_i = \sqrt{\varepsilon_i} = \sqrt{\varepsilon'_i + i\varepsilon''_i}$ of the two layers are then obtained from

$$n'_i = \left(\frac{1}{2}\left(\varepsilon'_i + \sqrt{\varepsilon'^2_i + \varepsilon''^2_i}\right)^{1/2}\right)$$

and $n''_i = \varepsilon''_i/2n'_i$, where the prime and double-prime functions indicate the amplitudes of the real and imaginary components. Consider a monochromatic plane wave $\vec{E}(\vec{r},t) = \vec{E}_0 e^{i(\vec{k}_1\vec{r}-\omega t)}$ propagating through the dielectric toward the metal. The plane of incidence is defined by $y = 0$, that is, $\vec{k}_1 = (k_x, 0, k_{1z}) = (\omega n_1/c)(\sin(\theta_1), 0, \cos(\theta_1))$, with θ_1 denoting the angle of incidence and c being the speed of light in vacuum. Snell's law gives $n_1 \sin(\theta_1) = n_2 \sin(\theta_2)$ and the continuity equations require that the wave vectors of the reflected and transmitted beams be given by $\vec{k}_{1\mathrm{r}} = (k_x, 0, -k_{1z})$ and $\vec{k}_2 = (k_x, 0, k_{2z}) = (\omega/c)(n_1 \sin(\theta_1), 0, n_2 \cos(\theta_2))$, respectively.

For s-polarized incident light, the electric field vector lies perpendicular to the plane of incidence and $\vec{E}_0 = (0, E_0, 0)$. The reflection and transmission coefficients ϱ_s and τ_s for the incident beam are given by Fresnel's equations [143, 144]

$$\varrho_s = \frac{1-a}{1+a}, \qquad \tau_s = \frac{2}{1+a}, \tag{5.27}$$

respectively, with $a = k_{2z}/k_{1z} = \tan(\theta_1)/\tan(\theta_2)$. In this case, the amplitudes of the reflected and transmitted fields are $\vec{E}_{0r} = \varrho_s \vec{E}_0$ and $\vec{E}_{0t} = \tau_s \vec{E}_0$, respectively.

For p-polarized incident light, $\vec{E}_0 = E_0(-\cos(\theta_1), 0, \sin(\theta_1))$ lies in the plane of incidence and Fresnel's equations give

$$\varrho_p = \frac{1-b}{1+b}, \qquad \tau_p = \frac{2(n_1/n_2)}{1+b} \tag{5.28}$$

with $b = (n_1/n_2)^2(k_{2z}/k_{1z}) = (n_1/n_2)^2 a$. The reflected and transmitted field amplitudes then are $\vec{E}_{0r} = \varrho_p E_0(\cos(\theta_1), 0, \sin(\theta_1))$ and $\vec{E}_{0t} = \tau_p \vec{E}_0(-\cos(\theta_2), 0, \sin(\theta_2))$, respectively. The resulting angle-dependent reflectance curves $R_{s,p}(\theta) = |\varrho_{s,p}|^2$ of an Ag/air interface irradiated with s- and p-polarized light at $\lambda = 1000$ nm ($\omega = 1.24$ eV) are shown in Figure 5.11.

In this case, $\omega \ll \omega_p$ so that the dielectric function of the metal is governed by its large and negative real part ($\varepsilon_2 = -51.1 + 0.943i$). Hence, the induced coherent polarization $\vec{P}$ of the electron gas is phase shifted by 180° with respect to the driving field. The electromagnetic field inside the metal is thus effectively screened and decays within the skin depth $\delta = \lambda/(2\pi\,\mathrm{Im}\,(n_2))$, which is about 25 nm for gold and silver in a fairly broad range of wavelengths from the visible up to the mid-infrared. In the present example, $\delta = 22$ nm. The second important consequence of the coherent free-carrier oscillation, that is, the same coherent polarization, is the almost loss-free specular reflection of the incident light wave. It is important to realize that s- and p-polarized light waves experience different phase shifts $\varphi = \arg(\varrho)$, and hence reflection from a metallic mirror at an off-normal angle of incidence modifies the polarization state of the reflected field.

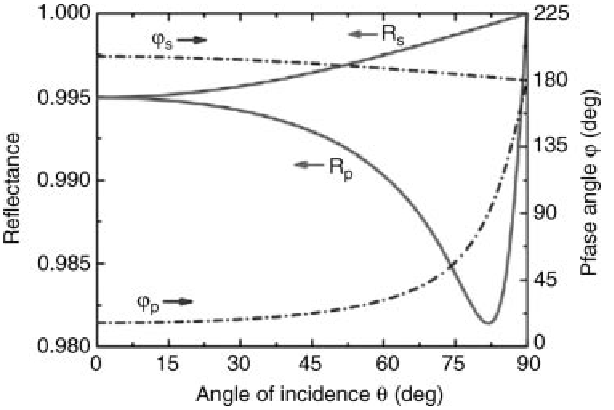

Figure 5.11 The reflectance and phase shift for the reflection of a light wave at $\lambda = 1000$ nm at a silver mirror. The dielectric function of silver is taken as $\varepsilon_2 = -51.1 + 0.943i$. The data are plotted for s- and p-polarized light as a function of the angle of incidence θ.

5.4.3
Surface Plasmon Polariton Fields

5.4.3.1 Planar Interfaces

It has been known since the pioneering work of Ritchie that metal/dielectric interfaces support collective charge density oscillations and surface plasmons [32, 145]. These surface charge oscillations couple strongly to light and the resulting coupled modes between charges and fields are termed surface plasmon polaritons (SPPs). Surface plasmon polaritons propagate freely along planar interfaces and are evanescently confined in the direction perpendicular to the interface. They penetrate into the dielectric on a scale given by their wavelength, whereas the skin depth gives their penetration depth into the metal. Throughout most of this depth, the dipolar charge oscillations preserve charge neutrality. A net charge density exists only within the Thomas–Fermi screening length of about 1 Å at the surface. For a perfectly planar surface, such SPP fields must have a finite component of the electric field normal to the surface; s-polarized SPP modes with an electric field vector oriented parallel to the surface do not exist [139, 142]. SPP modes on planar interfaces are necessarily p-polarized electromagnetic waves with a magnetic field vector $\vec{H}$ pointing parallel to the interface. Some of the fundamental SPP properties are readily derived directly from Maxwell's equations in the absence of external sources [130, 142].

We again consider a planar interface, located at $z = 0$, between a semi-infinite and a nonmagnetic metal in half-space $z < 0$, with a local dielectric function $\varepsilon_1(\omega)$ and a dielectric with $\varepsilon_2(\omega)$. The metallic layer is irradiated with a monochromatic wave of frequency ω propagating along the x-axis with vectors

$$\vec{E}_i = (E_{ix}, 0, E_{iz})\mathrm{e}^{-\kappa_i|z|}\,\mathrm{e}^{(ik_{ix}x-\omega t)}, \tag{5.29}$$

$$\vec{H}_i = \big(0, H_{iy}, 0\big)\mathrm{e}^{-\kappa_i|z|}\,\mathrm{e}^{(ik_{ix}x-\omega t)}, \tag{5.30}$$

where k_{ix} gives the component of the wave vector parallel to the interface in medium $i = 1, 2$. Ampère's law connects the electric and magnetic field amplitudes ($+$ sign for $i = 1$)

$$i\kappa_i H_{iy} = \pm\varepsilon_i\varepsilon_0\omega E_{ix}, \tag{5.31}$$

$$k_{ix} H_{iy} = -\varepsilon_i\varepsilon_0\omega E_{iz} \tag{5.32}$$

and hence gives $E_{ix}/E_{iz} = \pm\kappa_i/ik_{ix}$. It requires, together with Faraday's law, the magnitude of the wave vector components along the z-axis to be

$$\kappa_i = \sqrt{k_{ix}^2 - \varepsilon_i k_0^2} \tag{5.33}$$

with $k_0 = \omega/c$ being the magnitude of the light wave vector. Since the tangential components of E and H are continuous at the interface, $H_{1y} = H_{2y}$ and $E_{1x} = E_{2x}$. Equation (5.10) then gives the surface plasmon condition

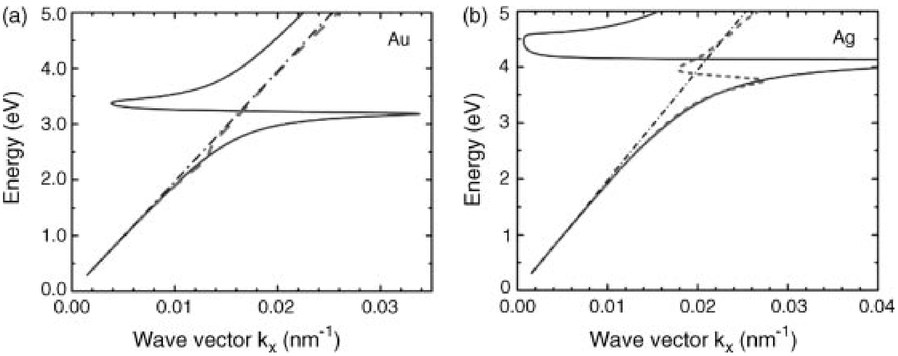

Figure 5.12 SPP dispersion relations $\omega(\mathrm{Re}\,(k_x))$ based on Eq. (5.35) for planar (a) gold/air and (b) silver/air interfaces. The curves are calculated based on the Drude model neglecting interband absorption ($\varepsilon_i = 0$, solid lines) and including interband absorption (dashed lines). The light line $\omega = c \cdot k_x$ is shown as a dash-dotted line.

$$\frac{\varepsilon_1}{\kappa_1} + \frac{\varepsilon_2}{\kappa_2} = 0. \tag{5.34}$$

The boundary conditions at the interface also demand the continuity of the tangential component of the wave vector $k_{1x} = k_{2x} = k_x$. Together with Eqs. (5.33) and (5.34), the continuity equation gives the surface plasmon dispersion relation for a planar interface [32]

$$k_x = \frac{\omega}{c}\left(\frac{\varepsilon_1\varepsilon_2}{\varepsilon_1 + \varepsilon_2}\right)^{1/2}. \tag{5.35}$$

The dispersion relations $\omega(\mathrm{Re}\,(k_x))$ are shown in Figure 5.12 for air/gold and air/silver interfaces. The curves have been calculated by using the Drude dielectric function (Eq. (5.10)) in the presence (dashed lines) and absence (solid lines) of interband absorption terms. For frequencies above the plasma frequency $\omega > \omega_\mathrm{p}$, $\mathrm{Re}\,(\varepsilon_1) > 0$ and the metal becomes transparent. In this region, the diagram displays the dispersion relation of light inside the metal. For sufficiently high frequencies, $\varepsilon_1 \rightarrow 1$ and the curve approaches the light line $\omega = c \cdot k_x$ (c is the speed of light in vacuum) indicated by a dash-dotted line. The high k_x asymptotic limit given by $\varepsilon_1 + \varepsilon_2 = 0$ defines the classical surface plasmon frequency, which in the case of a lossless Drude model for the dielectric function at a metal/air interface is $\omega_\mathrm{SP} = \omega_\mathrm{p}/\sqrt{2}$.

Of interest is the SPP dispersion relation at frequencies below ω_p. At sufficiently low frequencies, in the so-called retarded region, the SPP dispersion lies only slightly outside the light line. In the absence of interband screening, this region roughly covers the small wave vector part ($k_x < \omega_\mathrm{p}/(\sqrt{2c})$) of the dispersion curve at energies $\omega < \omega_\mathrm{SP} = \omega_\mathrm{p}/\sqrt{2}$. In this situation, SPPs are light-like quasi-particles, propagating at essentially the speed of light and having evanescent SPP field amplitudes (Eqs. (5.29) and (5.30)), which decay exponentially on either side of the interface. In this region, the spatial extent of the electromagnetic field is very different on the

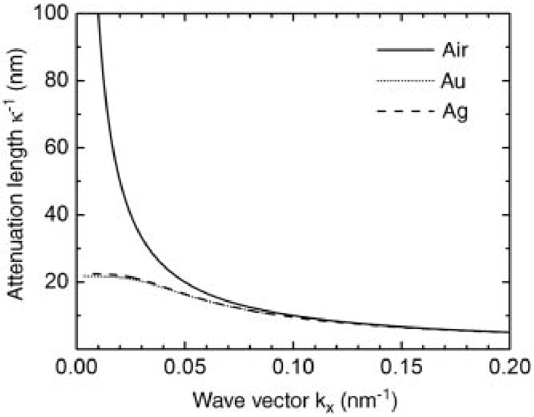

Figure 5.13 The attenuation lengths $l_i = |1/\kappa_i|$ of the electromagnetic field on either side of Au/air and Ag/air interfaces deduced from Eq. (5.34). An idealized loss-free Drude model ($\varepsilon_\infty = 1$, $\tau \to \infty$, $\varepsilon_i = 0$) is taken for the dielectric function of the metal. The solid black line shows the attenuation length l_1 in air, whereas the dotted and dashed lines denote l_2 in gold and silver, respectively.

two sides. Equations (5.34) and (5.35) give the following expression for the SPP decay constants k_i perpendicular to the interface:

$$\kappa_i = \frac{\omega}{c}\sqrt{\frac{-\varepsilon_i^2}{\varepsilon_1 + \varepsilon_2}}. \tag{5.36}$$

The resulting attenuation lengths $l_i = |1/\kappa_i|$ at which the electromagnetic field falls off to $1/e$ are shown in Figure 5.13. For clarity, values resulting from a only lossless Drude model are shown. In the long-wavelength limit ($q \to 0$), the attenuation length in the metal is given by the skin depth. The field on the air side, however, is much less confined and extends over more than $c/\omega = \lambda/(2\pi)$, with λ being the wavelength of light in vacuum. In this regime, the interface supports SPP modes, but the fields are only weakly confined to the interface and field localization effects are basically absent. Therefore, retardation effects arising from the finite SPP phase velocity are important for optical properties of the interface.

This changes in the nonretarded regime of large in-plane wave vectors $k_x > \omega_{\mathrm{SP}}/c$ in the frequency range $\omega < \omega_{\mathrm{SP}}$. Here, for a lossless Drude metal, the dispersion relation $\omega(k_x)$ is a monotonically increasing function of k_x that approaches asymptotically ω_{SP}. SPP waves in the nonretarded regime have interesting properties. Their in-plane wave vector k_x is much larger than that of a light wave of the same frequency. In the fictitious lossless case, the corresponding in-plane wavelength can be reduced to essentially arbitrarily small values. Therefore, SPP waves can be localized in volumes much smaller than λ^3, breaking the diffraction limit in conventional far-field optics. SPP waves in the nonretarded regime are strongly confined to the interface. It is seen in Figure 5.13 that the attenuation length in air becomes similar to that in the metal and approaches $1/k_x$ as ω approaches ω_{SP}. As $k_z \gg k_0$, the finite propagation speed of the SPP modes is of minor importance and quasi-static approximations of Maxwell's equations can describe the optical properties of nonretarded SPP modes reasonably well. Consequently, the magnetic field associated with nonretarded SPP waves is much weaker than that of a corresponding propagating field.

More important, since $k_x > k_0$, propagating light fields impinging on the interface cannot directly excite SPP modes. Coupling of far-field light to SPP at a metal/vacuum interface can occur in a total internal reflection geometry from a high-index substrate material for a thin metal film, creating evanescent fields at the interface, as demonstrated by Otto [146] and Kretschmann and Raether [147], or by scattering light off surface roughness or gratings, as pioneered by Teng and Stern [148]. In the latter approach, the scattering at a subwavelength asperity such as a sharp edge or a slit with smaller features, the wavelength of exciting light provides the necessary momentum to couple to the SPP modes [149]. Also, near-field excitation schemes, directly providing evanescent fields, can be employed [150]. Most recently, nonlinear four-wave mixing has been demonstrated as a versatile method for exciting SPP modes [151].

For real, that is, lossy metals, the situation is obviously less ideal. As illustrated in Figure 5.12, the finite imaginary part of ε_1 removes the singularity in Eq. (5.36) and hence limits the maximum value of Re (k_x), as well as the field confinement to the interface. For Im $(\varepsilon_1) \neq 0$, also the quasi-bound, leaky part of the dispersion relation with $\omega_{\mathrm{SP}} < \omega < \omega_{\mathrm{p}}$ is allowed. It is evident that for both gold and silver structures, the interband contribution to the dielectric function greatly affects the SPP modes in the visible range.

In case of a planar interface, the SPP dispersion is fully governed by the frequency-dependent dielectric function of the metal and the dielectric. It will be illustrated in Section 5.4.4.3 that structuring of the metal provides an additional degree of freedom for tailoring SPP dispersion and fields. This led to artificially designed surface plasmon resonances or, more precisely, the optical properties of structures supporting SPP fields by patterning metallic films with closely packed geometric arrangements of structures with dimensions and separations much smaller than the vacuum wavelength [152, 153]. This emerging field is now sometimes called designer or spoof plasmonics and evidently bears many similarities with other fields such as band gap engineering of semiconductors [154], or the design of photonic crystals [155] or metamaterials [156, 157].

An additional important consequence of Eq. (5.35) is the finite propagation length of SPP wave packets along planar interfaces. The finite extent of the SPP field into the metal results in damping of SPP waves due to unavoidable Ohmic losses. For a complex value of ε_1, the propagation constant k_x is also a complex number and the SPPs are damped with a propagation length $L_{\mathrm{d}} = 1/(2\,\mathrm{Im}\,(k_x))$. Typical propagation lengths are <10–100 μm in the visible spectrum for Ag films (Figure 5.14).

The propagation lengths increase greatly with longer wavelength due to the concomitant increase in k_2. For planar interfaces, the lengths can be increased further by sandwiching a thin metal film between the two dielectric layers. In these multilayers, SPPs at both interfaces are coupled giving rise to symmetric and

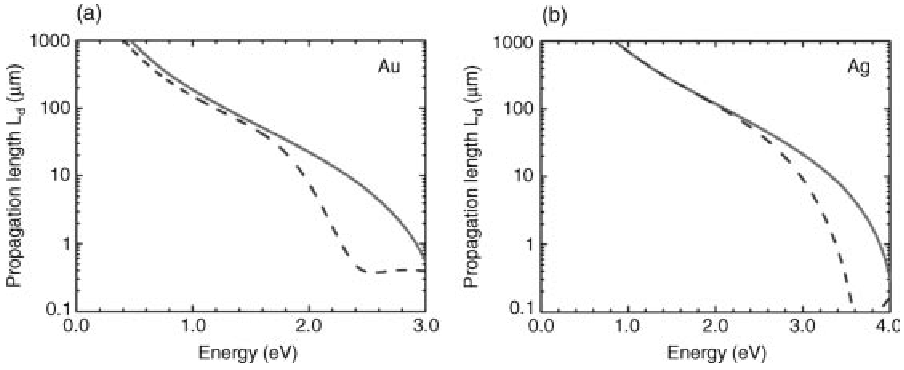

Figure 5.14 SPP propagation lengths $L_\mathrm{d} = 1/(2\,\mathrm{Im}\,(k_x))$ as a function of SPP energy calculated for (a) gold/air and (b) silver/air interfaces based on the dispersion relation (Eq. (5.33)) for Drude models neglecting ($\varepsilon_i = 0$, solid lines) and including interband absorption (dashed lines). The propagation lengths are plotted on a logarithmic scale.

antisymmetric modes. The antisymmetric modes have reduced Ohmic losses because they are only weakly confined to the metal. These long-range SPP solutions [158] show drastically increased propagation lengths, extending to the mm range. Attempts to geometrically pattern the metal surface will almost inevitably result in a reduction of the propagation length [159–162] because the collective charge oscillations in these geometrically confined metallic structures can now also emit radiation into the far field. Radiation damping therefore appears as an additional loss mechanism [163]. Hence, the reduction of SPP losses in passive or active hybrid metallic–dielectric nanostructures is a very active field of current research [164, 165].

The preceding description of SPPs is based on a local dielectric function $\varepsilon(\omega)$, independent of the SPP wave vector. Possible nonlocality of the electronic response and the microscopic spatial distribution of the electron density have been neglected. Such microscopic effects are thought to be of minor importance for sufficiently long SPP wavelengths $2\pi/k_x$, but will become important if the SPP wavelength approaches the Fermi wave vector, $k_x \approx k_\mathrm{F}$. For a detailed discussion, we recommend Ref. [142].

The SPP coupling at discontinuities and propagation in flat metal films can be imaged by near-field microscopy or photoemission electron microscopy (PEEM) [149, 166–168]. Such measurements rely on the interference between the external excitation field and the SPP wave packet generated at a vacuum/metal interface. Near-field microscopy has the advantage of being a linear technique, but it does not directly measure the total field present in the metal. By contrast, PEEM measurements detect the spatial distribution of two-photon photoemission, without introducing a near-field perturbation. Therefore, PEEM measurements provide a nonlinear map of the polarization gratings excited by different field components. Moreover, because PEEM in an imaging method, it is relatively simple to perform femtosecond time-resolved measurements on surface plasmon dynamics [169]. Proposals have been put forward to use PEEM in the attosecond domain in order to resolve plasmonic fields with a time resolution of less than one optical cycle [170].

5.4.4
Surface Plasmons in Nanostructured Metal Films

A fundamentally different approach for localizing electromagnetic fields at surfaces relies on the optical excitation of individual or coupled arrays of metallic nanoparticles. Metallic nanostructures of arbitrary shape show a strong optical response at certain resonance frequencies. This response is connected with a pronounced local enhancement of the electromagnetic field in the vicinity of the nanoparticle. Such enhancements are important in, for instance, light harvesting for solar conversion applications, or surface-enhanced spectroscopies, such as Raman spectroscopy, and surface photochemistry [171–173]. The optical properties of single metallic nanoparticles have already been discussed in textbooks and reviews [131, 132, 139, 174, 175], and only very basic properties will be summarized here as prototypical examples for how the interplay between metallic dielectric function and geometric shape gives rise to new optical properties and greatly enhanced local electromagnetic fields.

5.4.4.1 Spherical Nanoparticles

In the quasi-static approximation, the isotropic polarizability α of a spherical nanoparticle of radius a is found by solving the Laplace equation for the scalar potential Φ, $\Delta\Phi = 0$ [143], and is given as

$$\alpha = 4\pi a^3 \frac{\varepsilon_1 - \varepsilon_2}{\varepsilon_1 + 2\varepsilon_2} \tag{5.37}$$

for a metal particle described by ε_1 in an isotropic and nonabsorbing medium with dielectric constant ε_2.

An incident electromagnetic field $\vec{E}_0(\omega)$ will polarize the nanoparticle and create a spatially homogeneous field $\vec{E}_{\text{in}}(\omega) = (3\varepsilon_2/(\varepsilon_1 + 2\varepsilon_2))\vec{E}(\omega)$ inside the sphere. This approximation can be valid only for particles smaller in size than the skin depth because for larger particles $\vec{E}_{\text{in}}$ will necessarily decay in the interior of the sphere. The electromagnetic field $\vec{E}_{\text{out}} = \vec{E}_0 + \vec{E}_1$ outside the sphere is given as the sum of the incident field $\vec{E}_0(\omega)$ and the field $\vec{E}_1(\omega)$ that is reradiated by a fictitious point-like dipole located at the center of the sphere ($\vec{r} = 0$) and having a dipole moment

$$\vec{p}(\omega) = \varepsilon_2 \varepsilon_0 \alpha(\omega) \vec{E}_0(\omega). \tag{5.38}$$

For a monochromatic incident field at frequency ω, the field $\vec{E}_1(\vec{r}, t)$ at position $\vec{r}$ outside the sphere is thus given by

$$\vec{E}_1(\vec{r}, t) = \frac{1}{4\pi\varepsilon_2\varepsilon_0}\left[k^2(\vec{n} \times \vec{p}) \times \vec{n}\frac{\mathrm{e}^{ikr}}{r} + [3(\vec{n} \cdot \vec{p}) - \vec{p}]\left(\frac{1}{r^3} - \frac{ik}{r^2}\right)\mathrm{e}^{ikr}\right]\mathrm{e}^{-i\omega t} \tag{5.39}$$

with $\vec{n} = \vec{r}/|\vec{r}|$ and $k = \sqrt{\varepsilon_2}\omega/c$. The different symmetries of the optical near field given by the last two terms and the optical far field given by the first term in Eq. (5.39) are illustrated in Figure 5.15 for a particle with a 10 nm radius [176].

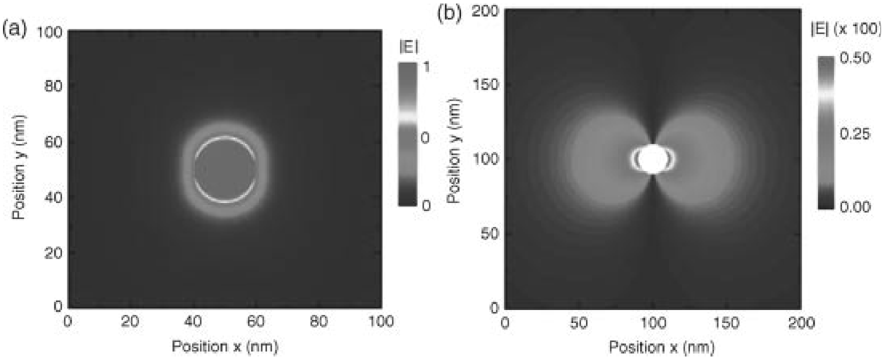

Figure 5.15 Magnitude of the electric field $|\vec{E}(\vec{r})|$ (arbitrary units) near a small nanoparticle with a radius of 10 nm. The field profile is calculated in the *x*–*y* plane using Eq. (5.39), assuming that it is given by that of a point-like oscillating dipole $\vec{p} = p_0 \cdot \vec{e}_y \cdot e^{i\omega t}$ at the center of the sphere. (b) Electric field magnitude $|\vec{E}(\vec{r})|$ given by the far-field term in Eq. (5.39). Close to the particle, the far-field amplitude is up to two orders of magnitude smaller than that of the corresponding near field. (Please find a color version of this figure on the color plates.)

The near field is preferentially oriented along the direction of the incident field, whereas the far field vanishes along the dipole axis. For such a small particle, the field intensity in the direct vicinity of the particle is up to 10 000 times larger than that given by the far-field term in Eq. (5.39). This is a manifestation of the large enhancement of the local field by the nanoparticle.

Equation (5.37) shows that the polarizability experiences a resonant enhancement if the magnitude of the denominator $|\varepsilon_1 + 2\varepsilon_2|$ tends toward zero. For a sufficiently small Im (ε_1), the resonance (Fröhlich) condition is simply $\mathrm{Re}(\varepsilon_1) = -2\varepsilon_2$ and the associated quasi-particle is known as the dipole surface plasmon. For a spherical particle, which has a lossless Drude dielectric function and is embedded in air, the condition is met for $\omega_0 = \omega_\mathrm{p}/\sqrt{3}$. With increasing ε_2, the resonance shifts to the red. Higher order resonances occur when [174]

$$l(\varepsilon_1) + (l+1)\varepsilon_2 = 0, \quad l = 1, 2, \ldots \tag{5.40}$$

These are the quadrupole ($l = 2$) and higher resonances.

Within this quasi-static model, the scattering cross section of the nanoparticle $C_\mathrm{sca}(\omega)$ is obtained by calculating the total radiated power emitted by the dipole and dividing it by the intensity of the incident plane wave:

$$C_\mathrm{sca}(\omega) = \frac{k^4}{6\pi}|\alpha(\omega)|. \tag{5.41}$$

Similarly, the absorption cross section $C_\mathrm{abs}(\omega)$ is obtained from the power $P_\mathrm{abs} = (\omega/2)\,\mathrm{Im}\left[\vec{p} \cdot \vec{E}_0^*\right]$ absorbed by a point dipole:

$$C_\mathrm{abs} = k\,\mathrm{Im}\,[\alpha(\omega)]. \tag{5.42}$$

The extinction cross section is given by the sum $C_\mathrm{ext} = C_\mathrm{sca} + C_\mathrm{abs}$.

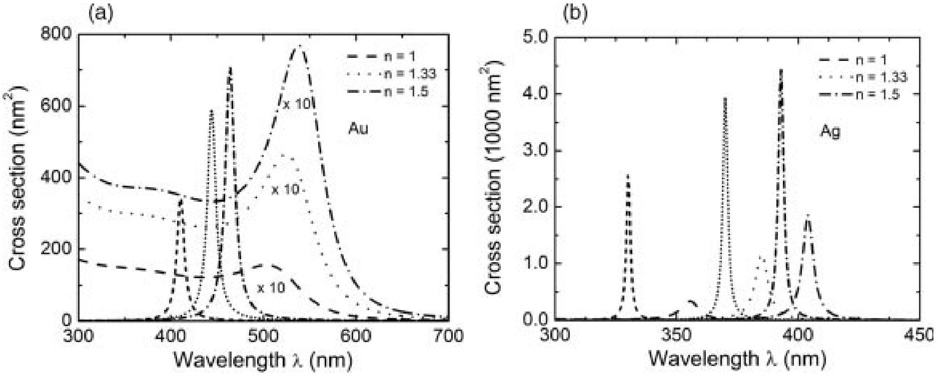

Figure 5.16 Absorption spectra $C_{abs}(\lambda)$ calculated using Eq. (5.42) for (a) spherical gold nanoparticles and (b) spherical silver particles with a radius of 5 nm embedded in different dielectric media with refractive indices $n = 1$, 1.33, and 1.5. The dielectric function of the metal is based on the dispersion relation (Eq. (5.35)) for Drude models neglecting ($\varepsilon_i = 0$, short dashed and dotted lines) and including (long dashed and dotted lines) interband absorption. The cross sections for gold particles in presence of interband damping have been enlarged by a factor of 10.

Absorption cross sections of gold and silver particles calculated for a Drude model in the absence of interband resonances and the full dielectric function in Eq. (5.10) are presented in Figure 5.16. The resonant enhancement depends critically on the details of the nanoparticle dielectric function (and of course its geometric shape) in the region around $\varepsilon_1 \approx -2\varepsilon_2$, making nanoparticle scattering spectra sensitive to the dielectric function of the environment [177]. This feature has been exploited in sensing applications [172].

The scaling of $C_{abs}(\omega)$ and $C_{sca}(\omega)$ with particle size is very different. The scattering cross section is proportional to $|\alpha|^2$ and hence to the sixth power of the particle radius, $C_{sca} \propto a^6$. By contrast, the absorption cross section scales only with a^3. This is immediately relevant for spectroscopic studies of individual nanoparticles, which are of particular importance for elucidating the complex interplay between nanoparticle size, shape, and environment on their optical properties. The scaling suggests that absorption studies are more sensitive to small particles than light scattering. Indeed photothermal imaging techniques have successfully detected individual sub-10 nm particles [178]. Light scattering from single small particles is challenging to resolve. After initial attempts to use near-field spectroscopic techniques [179], a variety of different far-field techniques, often relying on dark-field excitation schemes and combined with interferometric detection or nonlinear optical techniques, have been developed for this purpose [180–183]. PEEM-based measurements provide an alternative method for imaging emission from regions of high field enhancement that are associated with the excitation of plasmonic modes of metallic nanoparticles [169, 184, 185].

The quasi-static approach outlined above completely neglects the radiative damping of the particle dipole as well as retardation effects due to phase changes in the driving and scattered fields within the volume of the particle. Both effects are included in the rigorous electrodynamic model developed by Mie [132, 174].

Mie theory gives an approximate value for the polarizability of a sphere of volume V as [186, 187]

$$\alpha(\omega) = \frac{1-0.1\,(\varepsilon_1+\varepsilon_2)x^2}{((1/3)+\varepsilon_2/(\varepsilon_1-\varepsilon_2))-(1/30)(\varepsilon_1+10\varepsilon_2)x^2-i(4\pi^2\varepsilon_2^{3/2}/3)(V/\lambda^3)} \tag{5.43}$$

with $x = \pi a/\lambda$ being the size parameter and λ the vacuum wavelength. The new term in the numerator characterizes the retardation of the excitation field across the particle. The x^2 term in the denominator is due to the retardation of the depolarization field inside the particle [186]. Both terms lead to a spectral redshift of the resonance. The imaginary term in the denominator accounts for the radiation damping. Higher terms in x may be included in Eq. (5.43) and will lead to additional multipolar resonances in the spectra.

The radiation damping contributes to the finite lifetime T_2 of the photoinduced dipole moment $\vec{p}$ [188] and hence to a finite homogeneous linewidth $\Gamma = 2\hbar/T_2$ of the linear optical spectrum of a single nanoparticle. The radiative damping rate $1/T_{2,\mathrm{rad}} = \Gamma_{\mathrm{rad}}/2\hbar = \kappa V$ scales with the volume of the particle (κ is the proportionality coefficient) [132, 189, 190]. Therefore, the homogeneous spectral linewidth $\Gamma = \Gamma_{\mathrm{rad}} + \Gamma_{\mathrm{b}}$ of large spherical nanoparticles is expected to be larger than the linewidth Γ_{b} deduced within the quasi-static approximation and should increase with increasing particle diameter. The effect of particle size, geometry, and environment on Γ has been the subject of numerous primarily frequency domain studies of single metal nanoparticles during the last decade. For gold nanoparticles [189, 190], the linewidth Γ has indeed been found to increase from 200 meV ($T_2 = 6.5$ fs) for 20 nm particles to more than 800 meV ($T_2 = 1.7$ fs) for larger particles of more than 100 nm diameter. Values for the coefficient κ of $4 \times 10^{-7}\ \mathrm{fs}^{-1}\ \mathrm{nm}^{-3}$ to $6 \times 10^{-7}\ \mathrm{fs}^{-1}\ \mathrm{nm}^{-3}$ have been deduced [132, 189, 191]. For silver nanoparticles, a similar increase in linewidth has been reported [189, 191]. Solid agreement between the observed size dependence of Γ and Mie theory predictions based on ε values from Ref. [60] has been found. When reducing the size of the nanoparticle much below 50 nm, the contribution from radiative damping to the linewidth vanishes and the T_2 time approaches that deduced from quasi-static models. In this regime, for particle diameters between 50 and 20 nm, nonradiative contributions to the plasmon damping arising from intra- and interband electron–electron scattering, electron–phonon scattering, or impurity scattering dominate. Their effects on the dielectric function of a metal are discussed in more detail in Section 5.3.

When decreasing the particle diameter below 20 nm, the linewidth tends to increase again [132, 192, 193]. The linewidth increase is found to be inversely proportional to the particle radius, $\Gamma = \Gamma_{\mathrm{b}} + A \cdot a^{-1}$. Different microscopic mechanisms can contribute to this increase, in particular a reduction in the surface plasmon mean free path due to scattering at the nanoparticle surface [132, 194]. This modifies the decay of the surface plasmon into electron–hole pairs (Landau damping). In quantum mechanical terms, this is understood as an enhanced electron scattering induced by the quantum confinement of electronic states inside the nanoparticle [195, 196]. Also, the inelastic scattering of plasmon excitations at adsorbate or interface states (chemical interface damping) contributes [132, 187, 192, 197]. For particles with a well-controlled environment, for example, a defined dielectric shell, chemical interface damping can be suppressed and the effect of quantum confinement on surface plasmon damping can be quantitatively measured [193].

5.4.4.2 **Elliptical Nanoparticles**

To illustrate the effect of the shape of the particle on its optical properties, we briefly discuss nanoparticles whose shape in Cartesian coordinates is given by an ellipsoid of the form

$$\frac{x^2}{a_1^2}+\frac{y^2}{a_2^2}+\frac{z^2}{a_3^2}=1 \tag{5.44}$$

The principal axes are chosen such that $a_1 \leq a_2 \leq a_3$. In quasi-static approximation, the analytical solution for the polarizability tensor $\overleftrightarrow{\alpha}=\alpha_1\vec{e}_x+\alpha_2\vec{e}_y+\alpha_3\vec{e}_z$ is [174]

$$\alpha_i = 4\pi a_1 a_2 a_3 \frac{\varepsilon_1(\omega)-\varepsilon_2}{3\varepsilon_2+3L_i(\varepsilon_1(\omega)-\varepsilon_2)} \tag{5.45}$$

with $i=1,2,3$. The geometric factors L_i are

$$L_i=\frac{a_1 a_2 a_3}{2}\int_0^{\infty}\frac{\mathrm{d}q}{(a_i^2+q)f(q)} \tag{5.46}$$

with $f(q)=\sqrt{(q+a_1^2)(q+a_2^2)(q+a_3^2)}$. For spherical particles, $L_i=1/3$ and the sum rule $\sum_i L_i=1$ is fulfilled for all shapes. These polarizabilities can then be taken to calculate the fields $\vec{E}_1(\vec{r})$ near the outer surface of the ellipsoid by using Eq. (5.39) and $\vec{p}(\omega)=\varepsilon_2\varepsilon_0\overleftrightarrow{\alpha}(\omega)\vec{E}_0(\omega)$. This immediately gives the scattering and absorption cross sections of the nanoparticle following the same approach as outlined above.

The optical spectra of such particles hence depend critically on the orientation of the particle with respect to the incident field. This is best illustrated for prolate $(a_1=a_2<a_3)$ or oblate $(a_1<a_2=a_3)$ spheroidal particles having only two different nonzero elements of $\overleftrightarrow{\alpha}$ and hence showing two distinct spectral resonances in their optical spectra. For a prolate spheroid, the short-wavelength resonance is excited with incident light polarized along one of the short axes, whereas light polarized along the long axes couples to α_3. As illustrated in Figure 5.17, the resonance wavelength of α_3 is sensitive to the aspect ratio $r=a_3/a_1$ and gradually shifts to longer wavelengths as a_3 is increased. Also, an increase in aspect ratio greatly enhances the polarizability along the long axis and transforms the particle from an isotropic into a strongly anisotropic light scatterer, with its preferential polarization direction oriented along the long axis.

Variation in the shape of nanoparticles therefore is an important means to tailor their optical spectra. It affects not only the resonance energies but also the SP lifetimes [189]. SP dephasing times T_2 as long as 20 fs have been reported [189–191].

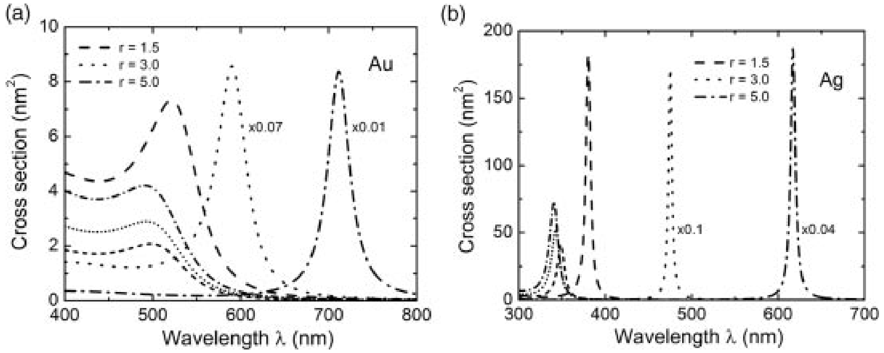

Figure 5.17 Simulations of absorption spectra $C_{\mathrm{abs}}(\lambda)$ of (a) elliptical gold and (b) elliptical silver nanoparticles with axes $a_1 = a_2 = 5$ nm and $a_3 = r \cdot 5$ nm. The short and long dashed and dotted lines lines represent spectra for light linearly polarized along the long and short axes, respectively. Interband absorption is included in the model for the dielectric function of the metal. With increasing ellipticity, the cross section for linearly polarized light along the long axes increases. The spectra have been scaled for clarity.

The radiative damping is weak and thought not to affect the T_2 time because the volume of the investigated nanoparticles is small. The comparatively long dephasing times are attributed to the suppression of interband absorption resulting from the redshift of the plasmon resonances. To first approximation, the electric field distribution in the vicinity of the particle is obtained from Eq. (5.39). Spatially resolved imaging of those fields may be achieved by different experimental techniques, including near-field scanning optical microscopy (NSOM) [175, 198–200], two-photon photoemission microscopy [169], tip-enhanced electron emission microscopy [201], cathodoluminescence imaging [202], or electron energy loss spectroscopy (EELS) [203]. Empirical extensions of the polarizability model given in Eq. (5.43) to larger sized elliptical nanoparticles have been discussed in the literature [192].

5.4.4.3 **Diffraction Gratings**

Diffraction gratings present another prime example illustrating the influence of the geometric shape of a metallic nanostructure on its optical properties. These have fascinated researchers since Wood published his observations on anomalous spectrally narrow dark bands in their reflectivity spectra [204, 205]. It took 40 years until Fano assigned these anomalies to the resonant excitation of surface waves [206], later termed surface plasmon polaritons. Renewed interest in diffraction gratings emerged in 1998 when Ebbesen *et al.* discovered the extraordinary enhancement of transmission of light through periodic two-dimensional arrays of subwavelength holes at certain resonance frequencies (Figure 5.18) [207]. To the surprise of many, they reported transmission coefficients much larger than $T = (64/27\pi^2)(kr)^4$, the so-called Bethe limit, for a normally incident plane with wavevector k through a single aperture with radius r in a perfectly conducting metal film [208, 209], and even exceeding the hole filling fraction.

A dominant effect of the grating in such experiments is to exchange momentum with the incident light beams. When scattering a monochromatic plane wave with

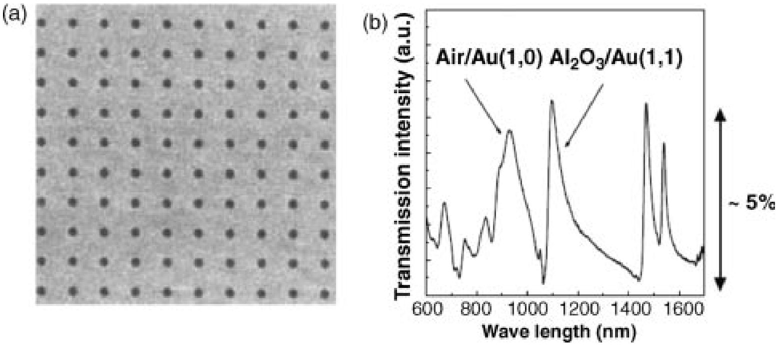

Figure 5.18 (a) Scanning electron microscope image of a periodic nanohole array in an optically thick gold film. The array period is 850 nm and the hole diameter 150 nm. (b) Representative far-field transmission spectrum through such an array in a gold film deposited on a sapphire substrate. The spectrum is recorded at near-normal incidence and transmission resonances at the air/gold or the sapphire/gold interface are indicated. Reprinted with permission from Ref. [210]. Copyright (2002), American Institute of Physics.

in-plane momentum $\vec{k}_{||} = \left(k_x, k_y, 0\right)$ off the grating, momentum conservation requires that the diffraction orders have in-plane wave vectors $\vec{k}_{p,q} = \vec{k}_{||} + p \cdot \vec{G}_x + q \cdot \vec{G}_y$. The integers p and q denote the diffraction orders and $\vec{G}_x = (2\pi/a_x)\vec{e}_x$ and $\vec{G}_y = \left(2\pi/a_y\right)\vec{e}_y$ are the reciprocal lattice vectors of a two-dimensional grating with periods $a_{x,y}$ along the x and y directions, respectively. Regular propagating diffraction orders are given if $|\vec{k}_{p,q}| \leq \omega/c$, that is, if the wave vector of the diffracted beam lies inside the light cone. Evanescent surface plasmon polariton fields can be excited at the grating interface if $\vec{k}_{p,q}$ lies outside the light cone, that is, if $|\vec{k}_{p,q}| > \omega/c$. Efficient grating coupling to SPP requires that energy and momentum conservation be fulfilled according to Eq. (5.35)

$$\omega(\vec{k}_{p,q}) = c \cdot |\vec{k}_{p,q}| \left(\frac{\varepsilon_1 + \varepsilon_2}{\varepsilon_1 \varepsilon_2}\right)^{1/2}. \tag{5.47}$$

Subwavelength diffraction gratings ($a_x, a_y < \lambda$) are of particular interest for coupling to SPP modes. In this case, close to normal incidence, only the zero-order mode with wave vector $k_{0,0}$ is a propagating mode, whereas all higher diffraction orders are evanescent SPP modes.

The resonance condition expressed in Eq. (5.47) gives approximate values for the transmission resonances in Figure 5.18 when considering that for thin transmission gratings deposited on a dielectric substrate, SPP modes can be excited either at the air side ($\varepsilon_2 = 1$) or at the dielectric side ($\varepsilon_2 = \varepsilon_\mathrm{d}$) of the grating. Consequently, different transmission resonances appear in Figure 5.18 for excitation of SPP modes at the air or the dielectric side. Excitation of SPP modes in diffraction gratings can be verified by mapping resonances in angle-resolved or spectrally resolved reflectivity measurements or, more directly, by microscopically imaging the resulting SPP fields. A representative NSOM image of the intensity of light transmitted through a two-dimensional array of nanoholes in a thin gold film is shown in Figure 5.19 [210].

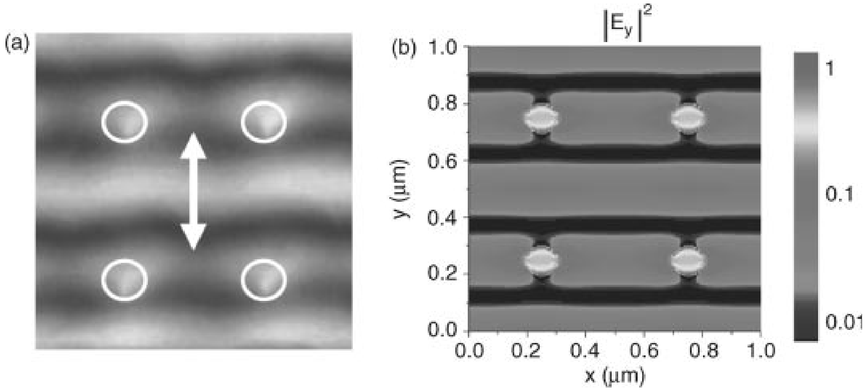

Figure 5.19 (a) NSOM image of the light transmitted through a subwavelength diffraction grating. The grating is fabricated by milling an 850 nm period array of 150 nm diameter nanoholes into a thin gold film deposited on a sapphire substrate. The grating is illuminated from the sapphire side with y-polarized light (see arrow) at 877 nm. The light at the air side of the grating is collected with a metal-coated NSOM fiber probe. Light regions correspond to high intensity, whereas the intensity drops to zero in the dark regions. Standing SPP waves at the grating interface are mapped. (b) Near-field intensity $|E_y|^2$ obtained from a three-dimensional finite difference time domain simulation. Reprinted with permission from Ref. [210]. Copyright (2002), American Institute of Physics. (Please find a color version of this figure on the color plates.)

The film thickness (about 100 nm) is much larger than the skin depth and hence is sufficient to fully suppress photon tunneling through the unstructured metallic film. The image reveals pronounced field intensity maxima in the region outside the holes (marked as white circles). The stripe-like pattern is oriented perpendicular to the polarization direction of the incident field, giving evidence for the excitation of longitudinal SPP modes. The clear standing wave pattern at the metal surface mainly results from the interference of SPP modes with wave vectors $\vec{k}_{||} = \pm\vec{G}_y$. A rotation of the incident polarization also changes the orientation of the standing wave pattern [210], giving additional support that these measurements probe SPP fields. The presence of the holes has different effects on the SPP fields propagating along the metal interface. They partly scatter the SPP field back into the far field and hence give rise to a radiative damping of the SPP modes [163]. Also, they scatter the SPP field into the holes. Photon tunneling couples the electromagnetic fields at the front and back sides of the film because electromagnetic waves do not propagate through subwavelength-sized cylindrical apertures [211]. This evanescent coupling between SPP fields at both interfaces is important for enhancing the transmission through the film and can be optimized by choosing identical dielectrics on both sides [211]. If air and dielectric modes are tuned into resonance, photon tunneling through the holes results in a coherent coupling between both modes and gives rise to the formation of new coupled SPP modes extending across both interfaces. This coupling leads to anticrossings between the interacting SPP resonances in angle-resolved linear optical spectra [212]. One contribution to the enhanced transmission, therefore, stems from the coupling of the incident light to SPP modes at the front side of the film, their coupling to evanescent modes inside the hole channels, and to SPP modes at the back side of the film and the outcoupling of the confined fields to the far field. This contribution is enhanced by tuning the excitation laser into resonance with the SPP modes. In addition, a certain fraction of the incident light can directly tunnel through the hole channels without coupling to SPP modes. Experimentally, both contributions can be readily distinguished in time-resolved pulse transmission experiments using ultrafast lasers with a pulse duration that is shorter than the SPP lifetime [213]. The linear optical transmission spectra are then given by the interference between the electric fields transmitted through the resonant SPP channel and the continuous direct transmission channel [214]˙ This interference gives rise to the asymmetric, Fano-like lineshapes shown in Figure 5.18b [215].

The scattering of SPPs at the holes also couples SPP modes on the same side of the metal film. The effect of this coupling on the linear optical spectra is readily seen in angle-resolved transmission spectra of an 150 nm thick gold film deposited on a sapphire substrate and perforated with an array of 50 nm wide slits with a period of 650 nm (Figure 5.20).

A clear anticrossing with a splitting of 70 meV is observed at angles of about 36° due to the coupling between SM[+1] and SM[−2] [For one-dimensional arrays, the allowed in-plane SPP wave vectors are $2\pi/a$, with a denoting the grating period. The SPP modes at the air and sapphire interface are then denoted as AM[p] and SM[p], respectively]. The coherent coupling between both modes thus leads to the opening of a band gap in the SPP dispersion relation. In addition, it results in a pronounced modification of the linewidths of the SPP resonances on the two sides of the crossing. The SPP coupling evidently affects the radiative lifetimes of the coupled modes because these linewidths are governed by the radiative SPP damping. This is qualitatively understood by considering the symmetries of the coupled modes. In the so-called strong coupling limit where the coupling strength is larger than the

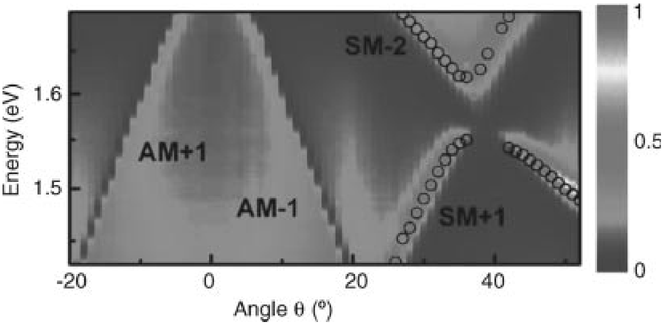

Figure 5.20 Experimentally measured angle-resolved transmission spectrum for a gold nanoslit array with a period of $a_0 = 650$ nm and a slit width of 50 nm. Open circles: Calculated SPP band structure near the crossing of SM[+1] and SM[−2] resonances. A band gap splitting of 72 meV is revealed. Note the spectral narrowing of the transmission spectrum and the decrease in transmission intensity in the lower energy region of the SM[+1]/SM[−2] crossing. (Please find a color version of this figure on the color plates.)

damping times of the individual resonances [216, 217], the coupling results in coupled SPP modes whose spatial mode profile is symmetric and antisymmetric with respect to the slit center [213]. As verified by near-field imaging, the spatial overlap of both modes with the slit scattering centers is very different and results in a very strong suppression of radiative damping for the antisymmetric mode [218]. Long SPP lifetimes exceeding 200 fs have been observed that exceed the SPP lifetimes of a perfectly flat metal/dielectric interface [213]. Hence, the coherent coupling between SPP modes not only provides a means to tailor the dispersion relations, but also manifestly alters the SPP lifetimes and the quality factors, as well as local field enhancements of nanoplasmonic resonators.

There have been numerous attempts to theoretically describe the phenomenon of extraordinarily enhanced transmission. For a very recent overview of the different approaches, the reader is referred to Ref. [219]. Initial attempts relied on semianalytical transfer matrix models, describing the metallic nanostructure as a special type of Fabry–Pérot resonator [211, 220]. Rather good agreement has been found between the experimental results of Ref. [210] and a fully vectorial diffraction model initially developed by Lochbihler [221] and later refined by Park and Lee [222]. Simulations based on this model as well as numerically demanding finite difference time domain simulations [223, 224] support the qualitative picture outlined above.

Numerous possible applications of such periodically structured metallic nanostructures have been discussed [141]. Of particular interest seem to be the directional transmission (beaming) of light through a single aperture flanked by periodic corrugations [225] and the ability to localize light in very small volumes, which is of interest for the sensing of single molecules [226].

5.4.4.4 **Adiabatic Metallic Tapers**

One of the most intriguing physical properties of metallic surface plasmon polariton waveguides is their ability to localize light in extremely small volumes, much below the diffraction limit. Here, we briefly discuss the optical properties of a specific SPP waveguide, a sharp, tapered gold tip, to highlight the interplay between geometrical shape and optical properties and to illustrate the unique light localization capabilities of such nanostructures that is advantageous for spectroscopic, sensing, and microscopic functions in both continuous wave and ultrafast measurements [200, 227, 228].

Consider a surface plasmon polariton wave packet propagating toward the apex of a conical metallic taper (Figure 5.21) with perfectly smooth interfaces. Owing to the evanescent nature of the SPP mode, this wave packet cannot emit radiation into the far field until it reaches the very apex of the taper. The taper apex acts as a scatterer for SPP waves and thus as a point-like light source. The optical properties of such conical tapers have been studied analytically by Babadjanyan *et al.* [230] and within the Wentzel–Kramers–Brillouin approximation [231] by Stockman *et al.* [232]. Several intriguing features of these results merit attention. First, the magnitude of the SPP in-plane wave vector $k \propto 1/r$ is inversely proportional to the distance r between a certain position on the taper surface and the tip apex. Correspondingly, the in-plane SPP wavelength tends to zero near the tip apex. Both phase and group velocities

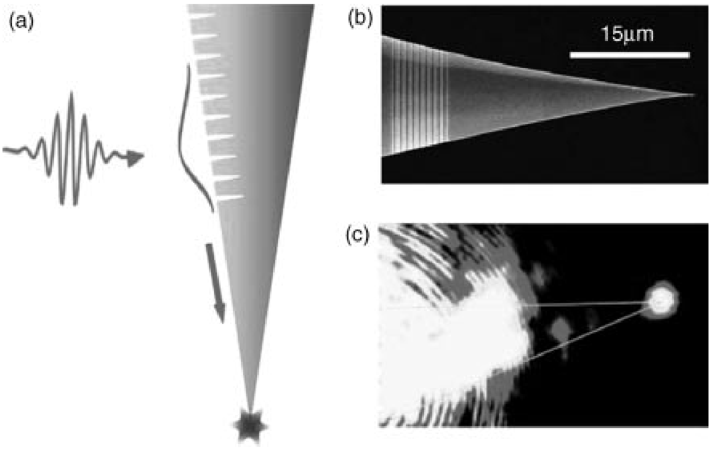

Figure 5.21 (a) Experimental geometry for adiabatic nanofocusing on conical gold tapers. Light from a tunable Ti:sapphire laser is focused by a high-NA objective onto a nanoslit grating milled onto the shaft of a gold taper. Grating coupling launches a SPP wave packet on the taper that propagates toward the tip apex, where it is scattered into the far field. (b) Scanning electron microscopy image of a chemically etched gold taper with a nanoslit grating patterned by focused ion beam milling. (c) Optical microscopy image of the light that is scattered from the tip apex after grating illumination. Reprinted with permission from Ref. [229]. Copyright (2007) American Chemical Society.

decrease to zero, and hence the SPP wave packet is predicted to be slowed down and come to a complete halt as it approaches the tip apex. The adiabatic decrease in group velocity is related to a divergence of the electric field strength near the tip apex and to an extreme concentration of the electromagnetic energy stored in the SPP wave packet into a vanishingly small spot size. Effectively, the spatial extent of the SPP wave packet reduces as it approaches the apex and is transformed adiabatically from a propagating into a localized mode. Even if the field singularity at the tip apex is removed by limiting the minimum tip radius to 2 nm [232], a strong enhancement of the field intensity by more than three orders of magnitude remains. This field localization is expected for adiabatic tapers whose change in taper diameter is small on a scale of the wavelength.

From this early work, the phenomenon of adiabatic nanocompression has received considerable theoretical and experimental attention. Different nanofocusing geometries including wedges [233, 234], cones [235–237], and nanogrooves [238] have been proposed and theoretically analyzed. On the experimental side, first the effect has been studied in two-dimensional tapered waveguides [239, 240]. A possible geometry for demonstrating adiabatic nanofocusing on conical tapers, introduced in Ref. [229], is shown in Figure 5.21 and consists of a chemically etched gold taper with an opening angle from 20° to 30°. The taper is patterned with a slit grating with a period of 800 nm and slit width of 150–300 nm. When illuminated with laser light and a wavelength approximately matching the grating period, a SPP wave packet is launched onto the taper shaft, propagating toward the tip apex. The 15–30 μm distance between the grating edge and the taper apex is chosen such that a significant fraction of the launched wave packet reaches the taper apex with minimal Ohmic loss or scattering into the far field. Only at the tip apex are the SPPs efficiently transformed into radiation. This is readily seen in microscope images taken from such tapers when illuminating the grating [229]. Apart from light scattering from the grating edges, the taper shaft remains dark, while a second and intense light spot is seen at the very apex of the tip. This was taken as indirect evidence for adiabatic nanofocusing on conical tapers. More direct evidence can be given by using such a localized nanoscale light spot at the apex as the light source in a scattering-type near-field scanning optical microscope [200, 227]. When scanning such a tip across a glass substrate covered with small gold metallic nanoparticles while illuminating the grating coupler, strong enhancement of the light scattered into the far field is seen when the tip is positioned directly on top of a nanoparticle (Figure 5.22).

The spatial resolution in these images is only of the order of 40 nm. The enhancement in scattering signal by a single 30 nm diameter particle is strong and amounts to more than 30% of the signal given by the light scattering from the tip apex in the absence of a nanoparticle [200]. This is considered direct evidence for the very efficient adiabatic focusing of far-field light toward a nanometer-sized spot at the tip apex. Such an essentially background-free high spatial resolution near-field scanning

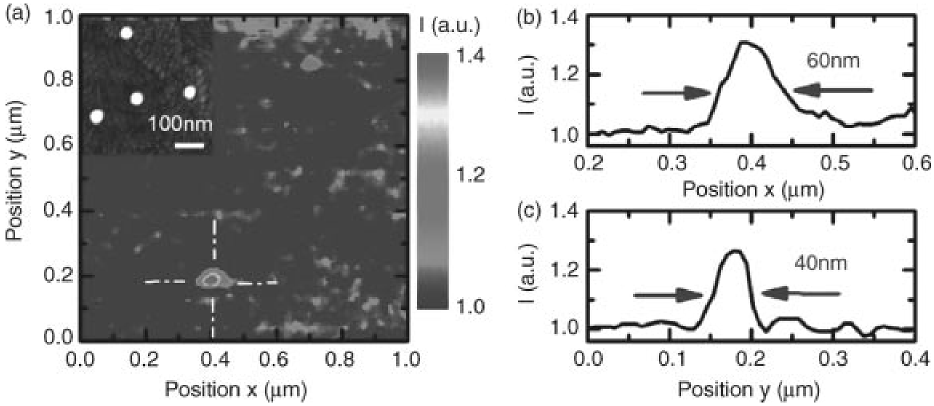

Figure 5.22 Two-dimensional optical images of individual gold nanoparticles on a glass substrate recorded by adiabatic nanofocusing scattering-type near-field scanning optical microscopy (s-NSOM). (a) Optical s-NSOM image of a single gold nanoparticle with <30 nm radius. In these experiments, SPP waves are launched onto a gold taper by grating coupling (Figure 5.21b) and the light scattering from the tip apex is recorded in the far field while scanning the tip across the surface of a dielectric substrate covered with a low concentration of gold nanoparticles. *Inset*: Scanning electron microscope image of the gold nanoparticles. (b) Cross sections of the optical intensity along the x and y directions (marked by dash-dotted lines in (a)). The optical resolution of about 40 nm and the large signal-to-background ratio confirm the efficient adiabatic nanofocusing of SPP waves at the tip apex. Reprinted with permission from Ref. [200]. Copyright (2011) American Chemical Society. (Please find a color version of this figure on the color plates.)

optical microscope is certainly of considerable interest for linear light scattering, Raman and fluorescence imaging of densely packed nanoparticle samples.

5.4.5
Exciton–Plasmon Coupling

So far, we have considered electromagnetic fields at the interface between a metal and a transparent dielectric and have focused on propagating or localized surface plasmon excitations. As all other electromagnetic waves, surface plasmons interact with materials such as semiconductors or molecules that may be present in the near field. When replacing the dielectric with a thin semiconducting layer or a layer of molecules, this layer may itself show optical absorption resonances in the spectral range of the surface plasmon resonances and therefore introduce resonant coupling between the modes. In case of low-dimensional, quantum-confined semiconductors, these resonances arise mostly from dipole-allowed excitonic excitations, optically induced electron–hole pairs bound by the Coulomb interaction [241–243]. In molecular layers, these are molecular excitons, arising from the light-induced transition of an electron from the highest occupied to the lowest unoccupied molecular orbital [244, 245].

In this case, an external light field not only can interact with the surface plasmon polaritons at the interface between the metal and its surrounding, but can also create excitons in the surrounding layer. Hence, the possibility for a resonant exchange of electromagnetic energy between excitons and surface plasmons exists. If this exciton–plasmon coupling is sufficiently strong, it will influence the optical properties of the coupled system. When the excitons are located close to the metal surface, that is, at distances of much less than one wavelength, the energy exchange will mainly be mediated by optical near fields (the last two terms in Eq. (5.39)). For larger distances, propagating fields (the first term in Eq. (5.39)) contribute and for very short distances of only a few angstroms, tunnel coupling of electrons and holes is expected to set in. The resulting charge transfer processes will not be considered here and we will restrict the discussion to electromagnetic couplings between the optically induced excitonic and surface plasmon dipole moments. In molecular systems, such dipole–dipole couplings are important for the excitation transfer in light harvesting systems [246]. Recently, they have also been investigated in coupled semiconductor quantum dot systems [247, 248].

An intuitive insight into the effects of such couplings on the optical properties of plasmonic systems can be gained from the hybridization model introduced by Nordlander and coworkers [249]. On the basis of earlier work [250, 251], the authors have investigated spherical metallic nanoshells covering small dielectric spheres. The theoretical work shows that the optical response of this composite system results from the electromagnetic interaction between the plasmon resonances of the individual constituents, in this case a metallic sphere and a spherical void inside a metallic film. The lowest order dipolar resonance of the sphere is discussed in Section 5.4.4.1. In quasi-static approximation, the polarizability of a spherical inclusion of radius a in a metal film with $\varepsilon_2(\omega)$ and filled with dielectric with ε_1

is given by exchanging ε_1 and ε_2 in Eq. (5.37) [132, 174]:

$$\alpha = 4\pi a^3 \frac{\varepsilon_2 - \varepsilon_1}{\varepsilon_2 + 2\varepsilon_1}. \tag{5.48}$$

Then, the Fröhlich condition for the SP resonance is $2\mathrm{Re}(\varepsilon_1) = \varepsilon_2$. This gives a SP resonance frequency $\omega_\mathrm{v} = \sqrt{(2/3)\omega_\mathrm{p}}$ in a lossless Drude model compared to $\omega_\mathrm{s} = \omega_\mathrm{p}/\sqrt{3}$ for the sphere. Using a hydrodynamic model for the SP response [252], it was shown that ω_v can be understood as the resonance frequency of a harmonic oscillator model for the collective charge density oscillation. The problem of finding the resonance of the hybrid system can then be transformed into solving coupled oscillator equations [252]. In this dipolar approximation, the resonance frequencies of the composite system are then derived as

$$\omega_\pm^2 = \frac{\omega_\mathrm{p}^2}{2}\left[1 \pm \frac{1}{3}\sqrt{1+8x^3}\right], \tag{5.49}$$

where $x = a/b$ defines the ratio of the inner and outer radii of the shell. This expression gives the same resonance frequencies as obtained from classical Mie scattering theory [132, 174]. For vanishingly small void volume, $x \to 0$, one retrieves the uncoupled resonances. With increasing void volume, the splitting between the resonances increases, indicating the formation of antisymmetrically coupled (antibonding) ω_+ plasmon mode and a symmetrically coupled (bonding) ω_- plasmon mode. The two modes correspond to out-of-phase and in-phase charge density oscillations at the inner and outer surfaces of the shell, respectively [249]. For sufficiently small x, the splitting between the modes can be approximated as $\omega_+ - \omega_- = \sqrt{(\omega_\mathrm{s} - \omega_\mathrm{v})^2 + 4|V|^2}$, giving a coupling energy (or Rabi splitting) [217, 231] of $\hbar V \approx \hbar\omega_\mathrm{p}(1/3)x^{3/2}$. If the coupling is sufficiently strong, the spectra of the composite particles show new resonances, which can be attributed to the coupled plasmon modes [249].

The same theoretical approach can be used to describe surface plasmon couplings in metallic dimers [253], multishell concentric spheres [249], or exciton–plasmon interactions [254]. When coating a metallic nanoshell with, for example, a thin layer of a J-aggregate molecular dye, the plasmonic excitations of the nanoshell can couple to the excitonic excitation of the molecular layer. This then leads to an exchange of electromagnetic energy between the excitonic and the plasmonic system and – for sufficiently strong coupling – as in the previous line to the formation of new coupled resonances with resonance frequencies that are spectrally shifted with respect to those of the uncoupled ones. J-aggregate dyes [245], formed by dissolving dye molecules, for example, 2,2′dimethyl-8-phenyl-5,6,5′,6′-dibenzothiacarbocyanine chloride (Figure 5.23a), at high concentration in polymer matrices are well suited for studies of exciton–plasmon interactions because of their large oscillator strengths and spectrally narrow absorption resonances (Figure 5.23b) [255].

The optical absorption spectra of ensembles of spherical silver and gold nanoparticles [257] and of gold nanoshells [254] covered with J-aggregate dye molecules have been studied experimentally. Spectral splittings of more than 100 meV have

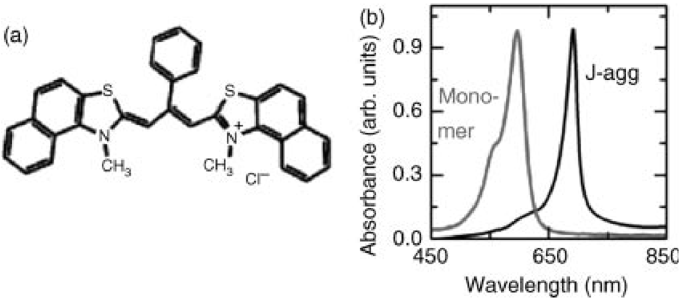

Figure 5.23 (a) Chemical structure of the cyanine dye 2,2′dimethyl-8-phenyl-5,6,5′,6′-dibenzothiacarbocyanine. (b) Room temperature optical absorption spectra of this dye in monomeric form (red line) and in J-aggregate form (black line). Reprinted with permission from Ref. [256]. Copyright (2010) American Chemical Society.

been observed [254] and taken as a signature of the coherent coupling between the plasmon excitations of the nanoparticle and the excitons of the J-aggregate complex. Since these splittings are less than the ensemble-averaged linewidth of the nanoshell absorption spectra, it is not yet clear whether the strong coupling regime, in which the coupling strength V is larger than the spectral width of the uncoupled resonances, can be reached in these systems [216, 217].

Clear evidence for strong exciton–plasmon coupling has been given for the coupling of J-aggregate excitons to surface plasmon polariton excitations on planar metallic films [258] and in one-dimensional nanoslit arrays [256] or two-dimensional hole arrays [259]. As an example, linear optical reflectivity spectra of a nanoslit grating in a gold film covered with a 50 nm thick J-aggregate dye layer are presented in Figure 5.24.

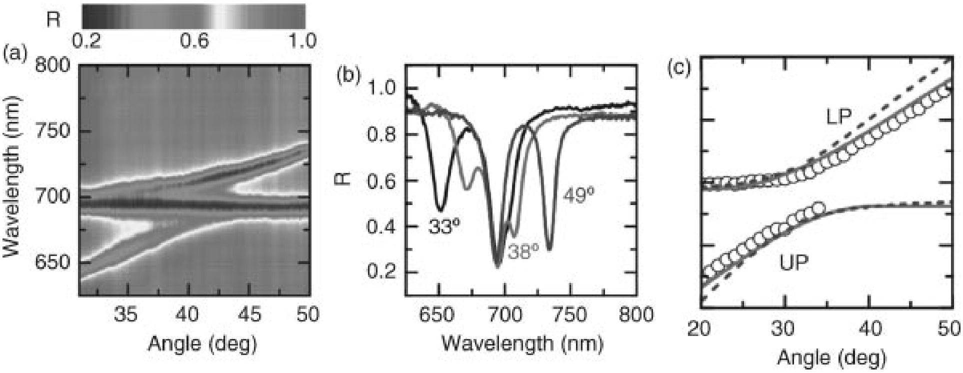

Figure 5.24 (a) Angle-resolved p-polarized linear reflectivity spectra ($T = 77$ K) of the J-aggregate dye deposited on a gold film perforated with a nanoslit grating of 430 nm period and 45 nm width. (b) Reflectivity spectra at different angles of 33°, 38°, and 49°. (c) Polariton dispersion relation obtained from the experimental spectra (open circles), a full vectorial solution of Maxwell's equations (solid line), and a coupled oscillator model (dashed line). Reprinted with permission from Ref. [256]. Copyright (2010) American Chemical Society. (Please find a color version of this figure on the color plates.)

The surface plasmon resonances of such gratings are discussed in Section 5.4.4.3. Here, the grating period of 430 nm was chosen such that the SPP resonance $\omega_{\mathrm{SPP}}(\theta)$ of the grating in the absence of exciton–plasmon coupling (Eq. (5.47)) is shifted from 650 to 750 nm when varying the angle of incidence θ between 30° and 50°. This allows one to angle tune the SPP resonance across the (angle-independent) exciton resonance ω_X of the dye. The width and the depth of the slits at 45 and 30 nm, respectively, were chosen to obtain spectrally narrow SPP resonances with a linewidth of less 10 nm. Near the crossing angle, $\omega_{\mathrm{SPP}}(\theta) = \omega_X$, a clear splitting of the optical spectra into upper and lower polariton resonances were observed. The resonance energies of the newly formed coupled polariton modes were found to be

$$\tilde{\omega}_{\mathrm{UP},LP} = \frac{1}{2}(\tilde{\omega}_X + \tilde{\omega}_{\mathrm{SPP}}) \pm \frac{1}{2}\sqrt{(\tilde{\omega}_X - \tilde{\omega}_{\mathrm{SPP}})^2 + 4V^2}, \tag{5.50}$$

where $\tilde{\omega}_{X,\mathrm{SPP}} = \omega_{X,\mathrm{SPP}} - i\gamma_{X,\mathrm{SPP}}$ denote the complex eigenfrequencies of the uncoupled exciton and SPP resonances. Equation (5.50) matches the observed dispersion relation when choosing a coupling energy of $\hbar V \approx 55$ meV, which was larger than the widths $\hbar\gamma_X$ and $\hbar\gamma_{\mathrm{SPP}}$ of both uncoupled resonances, confirming that the regime of strong exciton–SPP coupling was indeed reached in these experiments. The Rabi splitting $V = \int \vec{\mu}_X(\bar{r}) \cdot \vec{E}_{\mathrm{SPP}}(\bar{r})\,\mathrm{d}\bar{r}$ reflects the overlap integral between the excitonic transition dipole moment density $\vec{\mu}_X(\vec{r})$ and the electric field vector $\vec{E}_{\mathrm{SPP}}(\vec{r})$ of the local SPP mode and therefore measures the rate of exchange of electromagnetic energy between excitons and SPPs. The observation of such large coupling energies is of interest because the coupling and the optical properties of such hybrid structures can be altered by externally manipulating $\vec{\mu}_X(\vec{r})$ or $\vec{E}_{\mathrm{SPP}}(\vec{r})$. Owing to the short anticipated lifetimes of the coupled polariton modes, this provides a new degree of freedom for control of optical properties on fast timescales and potentially also small length scales. This functionality might be of interest for future applications in all-optical switching or nanolasing.

5.4.6
Summary

Electromagnetic fields at the interface between a metal and a dielectric are strongly confined to the interface. The coupling between an incident light field and collective charge density oscillations inside the metal results in propagating surface plasmon polariton and localized surface plasmon modes. These modes are fundamentally interesting because they allow the efficient localization of light on the nanoscale, in dimensions that are substantially smaller than the wavelength of light. For simple geometries such as planar interfaces, gratings, or spherical and elliptical nanoparticles, the local electromagnetic fields and the resulting linear optical properties of these structures are reasonably well understood using phenomenological Drude-like models for the local dielectric function of the metal. More complex geometries such as two- or three-dimensional arrays or nanometer-sized taper waveguides carry the potential to act as antennas or waveguides, providing exquisite and unprecedented control of the propagation and localization of light on the nanoscale. Such structures for localization of light on the nanometer scale are interesting for spectroscopic and dynamical imaging of single molecules, sensing, and inducing linear and nonlinear photochemistry of adsorbed molecules. Hybrid nanostructures consist of metals and gain materials add nonlinear ultrafast switching functionality and open the door to a new class of functional nanophotonic devices. A microscopic understanding of their optical properties requires knowledge about the spatiotemporal dynamics of electromagnetic fields near interfaces on short, nanometer-sized length and extremely fast atto- to femtosecond timescales, posing considerable experimental and theoretical challenges. We believe that emerging advances in ultrafast optical and electron microscopy in combination with advanced quantum theoretical modeling will provide more insights in the near future.

References

1 Davydov, A.S. (1976) *Quantum Mechanics*, Pergamon Press.

2 Bassani, F. and Parravicini, G.P. (1975) in *Electronic States and Optical Transitions in Solids* (ed. R.A. Ballinger), Pergamon Press, Oxford.

3 Ehrenreich, H. and Cohen, M.H. (1959) *Phys. Rev.*, **115**, 786.

4 Feibelman, P.J. (1982) *Prog. Surf. Sci.*, **12**, 287.

5 Weaver, J.H., Krafka, C., Lynch, D.W., and Koch, E.E. (1981) *Physics Data: Optical Properties of Metals*, Fachinformationszentrum Energie, Physik, Mathematik GmbH, Karlsruhe.

6 Krasovskii, E.E. and Schattke, W. (2001) *Phys. Rev. B*, **63**, 235112.

7 Krasovskii, E.E. and Schattke, W. (1999) *Phys. Rev. B*, **60**, R16251.

8 Adler, S.L. (1962) *Phys. Rev.*, **126**, 413.

9 Dietz, R.E., McRae, E.G., and Weaver, J.H. (1980) *Phys. Rev. B*, **21**, 2229.

10 Hedin, L. and Lundqvist, S. (1970) in *Solid State Physics*, vol. 23 (eds. D.T. Frederick Seiz and E. Henry), Academic Press, p. 1.

11 Hybertsen, M.S. and Louie, S.G. (1986) *Phys. Rev. B*, **34**, 5390.

12 Hanke, W. and Sham, L.J. (1980) *Phys. Rev. B*, **21**, 4656.

13 Albrecht, S., Reining, L., Del Sole, R., and Onida, G. (1998) *Phys. Rev. Lett.*, **80**, 4510.

14 Rohlfing, M. and Louie, S.G. (2000) *Phys. Rev. B*, **62**, 4927.

15 Benedict, L.X. and Shirley, E.L. (1999) *Phys. Rev. B*, **59**, 5441.

16 Chiodo, L., García-Lastra, J.M., Iacomino, A., Ossicini, S., Zhao, J., Petek, H., and Rubio, A. (2010) *Phys. Rev. B*, **82**, 045207.

17 Arnaud, B., Lebègue, S., Rabiller, P., and Alouani, M. (2006) *Phys. Rev. Lett.*, **96**, 026402.

18 Onida, G., Reining, L., and Rubio, A. (2002) *Rev. Mod. Phys.*, **74**, 601.

19 Hufner, S. (1995) *Photoelectron Spectroscopy: Principles and Applications*, Springer, Berlin.

20 Schattke, W. and Van Hove, M.A. (2003) *Solid-State Photoemission and Related Methods*, Wiley-VCH Verlag GmbH, Berlin.

21 Krasovskii, E.E., Silkin, V.M., Nazarov, V.U., Echenique, P.M., and Chulkov, E.V. (2010) *Phys. Rev. B*, **82**, 125102.

22 Krasovskii, E.E., Rossnagel, K., Fedorov, A., Schattke, W., and Kipp, L. (2007) *Phys. Rev. Lett.*, **98**, 217604.

23 Kane, E.O. (1964) Implications of crystal momentum conservation in photoelectric emission for band-structure measurements. *Phys. Rev. Lett.*, **12**, 97.

24 Feibelman, P.J. and Eastman, D.E. (1974) *Phys. Rev. B*, **10**, 4932.

25 Smith, N.V., Thiry, P., and Petroff, Y. (1993) *Phys. Rev. B*, **47**, 15476.

26 Reinert, F., Nicolay, G., Schmidt, S., Ehm, D., and Hüfner, S. (2001) *Phys. Rev. B*, **63**, 115415.

27 Vergniory, M.G., Pitarke, J.M., and Echenique, P.M. (2007) *Phys. Rev. B*, **76**, 245416.

28 Chen, Y., García de Abajo, F.J., Chassé, A., Ynzunza, R.X., Kaduwela, A.P., Van Hove, M.A., and Fadley, C.S. (1998) *Phys. Rev. B*, **58**, 13121.

29 García de Abajo, F.J., Van Hove, M.A., and Fadley, C.S. (2001) *Phys. Rev. B*, **63**, 075404.

30 Dil, J.H. (2009) *J. Phys. Condens. Matter*, **21**, 403001.

31 Kimura, A. *et al.* (2010) *Phys. Rev. Lett.*, **105**, 076804.

32 Ritchie, R.H. and Eldridge, H.B. (1962) *Phys. Rev.*, **126**, 1935.

33 Winkelmann, A., Hartung, D., Engelhard, H., Chiang, C.T., and Kirschner, J. (2008) *Rev. Sci. Instrum.*, **79**, 083303.

34 Baumgarten, L., Schneider, C.M., Petersen, H., Schäfers, F., and Kirschner, J. (1990) *Phys. Rev. Lett.*, **65**, 492.

35 Chiang, C.-T., Winkelmann, A., Yu, P., and Kirschner, J. (2009) *Phys. Rev. Lett.*, **103**, 077601.

36 Kiss, T. *et al.* (2005) *Phys. Rev. Lett.*, **94**, 057001.

37 Petek, H. and Ogawa, S. (1997) *Prog. Surf. Sci.*, **56**, 239.

38 Weinelt, M. (2002) *J. Phys. Condens. Matter*, **14**, R1099.

39 Chulkov, E.V., Borisov, A.G., Gauyacq, J.P., Sánchez-Portal, D., Silkin, V.M., Zhukov, V.P., and Echenique, P.M. (2006) *Chem. Rev.*, **106**, 4160.

40 Ge, N.-H., Wong, C.M., Lingle, R.L., Jr., McNeill, J.D., Gaffney, K.J., and Harris, C.B. (1998) *Science*, **279**, 202.

41 Andrianov, I., Klamroth, T., Saalfrank, P., Bovensiepen, U., Gahl, C., and Wolf, M. (2005) *J. Chem. Phys.*, **122**, 234710.

42 Ferrini, G., Giannetti, C., Galimberti, G., Pagliara, S., Fausti, D., Banfi, F., and Parmigiani, F. (2004) *Phys. Rev. Lett.*, **92**, 256802.

43 Bisio, F., Nývlt, M., Franta, J., Petek, H., and Kirschner, J. (2006) *Phys. Rev. Lett.*, **96**, 087601.

44 Pontius, N., Sametoglu, V., and Petek, H. (2005) *Phys. Rev. B*, **72**, 115105.

45 Himpsel, F.J. and Fauster, T. (1984) *J. Vac. Sci. Technol. A*, **2**, 815.

46 Claessen, R., Burandt, B., Carstensen, H., and Skibowski, M. (1990) *Phys. Rev. B*, **41**, 8270.

47 Schattke, W., Krasovskii, E.E., Díez Muiño, R., and Echenique, P.M. (2008) *Phys. Rev. B*, **78**, 155314.

48 Shudo, K. and Munakata, T. (2001) *Phys. Rev. B*, **63**, 125324.

49 Winkelmann, A., Lin, W.-C., Chiang, C.-T., Bisio, F., Petek, H., and Kirschner, J. (2009) *Phys. Rev. B*, **80**, 155128.

50 Winkelmann, A., Chiang, C.-T., Tusche, C., Ünal, A.A.,Kubo, A., Wang, L., and PetekA., H. (2012) Ultrafast multiphoton photoemission microscopy of solid surfaces in the real and reciprocal space, chapter in Dynamics of interfacial electron and excitation transfer in solar energy conversion: theory and experiment, (ed. P. Piotrowiak), Royal Society of Chemistry, London.

51 Ehrenreich, H. and Philipp, H.R. (1962) *Phys. Rev.*, **128**, 1622.

52 Smith, J.B. and Ehrenreich, H. (1982) *Phys. Rev. B*, **25**, 923.

53 Bonn, M., Denzler, D.N., Funk, S., Wolf, M., Wellershoff, S.S., and Hohlfeld, J. (2000) *Phys. Rev. B*, **61**, 1101.

54 Del Fatti, N., Bouffanais, R., Vallée, F., and Flytzanis, C. (1998) *Phys. Rev. Lett.*, **81**, 922.

55 Sjodin, T., Petek, H., and Dai, H.-L. (1998) *Phys. Rev. Lett.*, **81**, 5664.

56 Del Fatti, N., Voisin, C., Achermann, M., Tzortzakis, S., Christofilos, D., and Vallée, F. (2000) *Phys. Rev. B*, **61**, 16956.

57 Timm, C. and Bennemann, K.H. (2004) *J. Phys. Condens. Matter*, **16**, 661.

58 Stahrenberg, K., Herrmann, T., Wilmers, K., Esser, N., Richter, W., and Lee, M.J.G. (2001) *Phys. Rev. B*, **64**, 115111.

59 Liebsch, A. (1997) *Electronic Excitations at Metal Surfaces*, Plenum, New York.

60 Johnson, P.B. and Christy, R.W. (1972) *Phys. Rev. B*, **6**, 4370.

61 Hao, Z., Dadap, J.I., Knox, K.R., Yilmaz, M.B., Zaki, N., Johnson, P.D., and Osgood, R.M. (2010) *Phys. Rev. Lett.*, **105**, 017602.

62 Cavanagh, R.R., King, D.S., Stephenson, J.C., and Heinz, T.F. (1993) *J. Phys. Chem.*, **97**, 786.

63 Cooper, B.R., Ehrenreich, H., and Philipp, H.R. (1965) *Phys. Rev.*, **138**, A494.

64 Miller, T., Hansen, E.D., McMahon, W.E., and Chiang, T.C. (1997) *Surf. Sci.*, **376**, 32.

65 Cazalilla, M.A., Dolado, J.S., Rubio, A., and Echenique, P.M. (2000) *Phys. Rev. B*, **61**, 8033.

66 Marini, A., Del Sole, R., and Onida, G. (2002) *Phys. Rev. B*, **66**, 115101.

67 Marini, A. and Del Sole, R. (2003) *Phys. Rev. Lett.*, **91**, 176402.

68 Gumhalter, B., Lazić, P., and Došlić, N. (2010) *Phys. Status Solidi B*, **247**, 1907.

69 Rosei, R. (1974) *Phys. Rev. B*, **10**, 474.

70 Yu, P.Y. and Cardona, M. (2003) *Fundamentals of Semiconductors*, Springer, Berlin.

71 Miller, T., McMahon, W.E., and Chiang, T.C. (1996) *Phys. Rev. Lett.*, **77**, 1167.

72 Allen, J.W. and Mikkelsen, J.C. (1977) *Phys. Rev. B*, **15**, 2952.

73 Rakić, A.D., Djurišić, A.B., Elazar, J.M., and Majewski, M.L. (1998) *Appl. Opt.*, **37**, 5271.

74 Fischer, N., Schuppler, S., Fischer, R., Fauster, T., and Steinmann, W. (1993) *Phys. Rev. B*, **47**, 4705.

75 Schmidt, A.B., Pickel, M., Wiemhofer, M., Donath, M., and Weinelt, M. (2005) *Phys. Rev. Lett.*, **95**, 107402.

76 Pickel, M., Schmidt, A.B., Giesen, F., Braun, J., Minár, J., Ebert, H., Donath, M., and Weinelt, M. (2008) *Phys. Rev. Lett.*, **101**, 066402.

77 Bovensiepen, U. (2007) *J. Phys. Condens. Matter*, **19**, 083201.

78 Lisowski, M., Loukakos, P.A., Bovensiepen, U., Stähler, J., Gahl, C., and Wolf, M. (2004) *App. Phys. A*, **78**, 165.

79 Weinelt, M., Schmidt, A.B., Pickel, M., and Donath, M. (2007) *Prog. Surf. Sci.*, **82**, 388.

80 Palik (ed.) (1998) *Handbook of Optical Constants of Solids*, Academic Press, New York.

81 Drude, P. (1900) *Ann. Phys.*, **306**, 566.

82 Bethe, H.A. and Sommerfeld, A. (1967) *Elektronentheorie der Metalle*, Springer, Berlin.

83 Ashcroft, N.W. and Mermin, N.D. (1976) *Solid State Physics*, Holt, New York.

84 Youn, S.J., Rho, T.H., Min, B.I., and Kim, K.S. (2007) *Phys. Status Solidi B*, **244**, 1354.

85 Smith, N.V. (2001) *Phys. Rev. B*, **64**, 155106.

86 Ogawa, S., Nagano, H., and Petek, H. (1997) *Phys. Rev. B*, **55**, 10869.

87 Fann, W.S., Storz, R., Tom, H.W.K., and Bokor, J. (1992) *Phys. Rev. B*, **46**, 13592.

88 Sakaue, M., Kasai, H., and Okiji, A. (2011) *J. Phys. Soc. Jpn.*, **69**, 160.

89 Petek, H., Nagano, H., Weida, M.J., and Ogawa, S. (2000) *Chem. Phys.*, **251**, 71.

90 Altarelli, M., Dexter, D.L., Nussenzveig, H.M., and Smith, D.Y. (1972) *Phys. Rev. B*, **6**, 4502.

91 Beach, R.T. and Christy, R.W. (1977) *Phys. Rev. B*, **16**, 5277.

92 Parkins, G.R., Lawrence, W.E., and Christy, R.W. (1981) *Phys. Rev. B*, **23**, 6408.

93 Basov, D.N. and Timusk, T. (2005) *Rev. Mod. Phys.*, **77**, 721.

94 Littlewood, P.B. and Varma, C.M. (1991) *J. Appl. Phys.*, **69**, 4979.

95 Quinn, J.J. (1962) *Phys. Rev.*, **126**, 1453.

96 Gasparov, V.A. and Huguenin, R. (1993) *Adv. Phys.*, **42**, 393.

97 Echenique, P.M., Pitarke, J.M., Chulkov, E.V., and Rubio, A. (2000) *Chem. Phys.*, **251**, 1.

98 Marini, A., Onida, G., and Del Sole, R. (2001) *Phys. Rev. Lett.*, **88**, 016403.

99 Allen, P.B. (1971) *Phys. Rev. B*, **3**, 305.

100 Götze, W. and Wölfle, P. (1972) *Phys. Rev. B*, **6**, 1226.

101 Varma, C.M. (1997) *Phys. Rev. B*, **55**, 14554.

102 Mori, T., Nicol, E.J., Shiizuka, S., Kuniyasu, K., Nojima, T., Toyota, N., and Carbotte, J.P. (2008) *Phys. Rev. B*, **77**, 174515.

103 Cisneros, G. and Helman, J.S. (1982) *Phys. Rev. B*, **25**, 6504.

104 Li, H.Y., Zhou, S.M., Li, J., Chen, Y.L., Wang, S.Y., Shen, Z.C., Chen, L.Y., Liu, H., and Zhang, X.X. (2001) *Appl. Opt.*, **40**, 6307.

105 Gurzhi, R.N. (1957) *Zh. Eksp. Teor. Fiz.*, **33**, 660.

106 Lawrence, W.E. and Wilkins, J.W. (1973) *Phys. Rev. B*, **7**, 2317.

107 Quinn, J.J. and Ferrell, R.A. (1958) *Phys. Rev.*, **112**, 812.

108 Hofmann, P., Rose, K.C., Fernandez, V., Bradshaw, A.M., and Richter, W. (1995) *Phys. Rev. Lett.*, **75**, 2039.

109 Stahrenberg, K., Herrmann, T., Esser, N., and Richter, W. (2000) *Phys. Rev. B*, **61**, 3043.

110 Sun, L.D., Hohage, M., Zeppenfeld, P., Balderas-Navarro, R.E., and Hingerl, K. (2003) *Phys. Rev. Lett.*, **90**, 106104.

111 Harl, J., Kresse, G., Sun, L.D., Hohage, M., and Zeppenfeld, P. (2007) *Phys. Rev. B*, **76**, 035436.

112 Urbach, L.E., Percival, K.L., Hicks, J.M., Plummer, E.W., and Dai, H.L. (1992) *Phys. Rev. B*, **45**, 3769.

113 Fauster, T., Weinelt, M., and Höfer, U. (2007) *Prog. Surf. Sci.*, **82**, 224.

114 Güdde, J., Rohleder, M., Meier, T., Koch, S.W., and Höfer, U. (2007) *Science*, **318**, 1287.

115 Becker, M., Crampin, S., and Berndt, R. (2006) *Phys. Rev. B*, **73**, 081402.

116 Vergniory, M.G., Pitarke, J.M., and Crampin, S. (2005) *Phys. Rev. B*, **72**, 193401.

117 Ünal, A.A., Tusche, C., Ouazi, S., Wedekind, S., Chiang, C.-T., Winkelmann, A., Sander, D., Henk, J., and Kirschner, J. (2011) *Phys. Rev. B*, **84**, 073107.

118 Volokitin, A.I. and Persson, B.N.J. (1995) *Phys. Rev. B*, **52**, 2899.

119 Dvorak, J. and Dai, H.-L. (2000) *J. Chem. Phys.*, **112**, 923.

120 Ogawa, S., Nagano, H., Petek, H., and Heberle, A.P. (1997) *Phys. Rev. Lett.*, **78**, 1339.

121 Petek, H., Weida, M.J., Nagano, H., and Ogawa, S. (2000) *Science*, **288**, 1402.

122 Zhao, J. *et al.* (2008) *Phys. Rev. B*, **78**, 085419.

123 Wang, L.-M., Sametoglu, V., Winkelmann, A., Zhao, J., and Petek, H. (2011) *J. Phys. Chem. A*, **115**, 9479.

124 Weik, F., de Meijere, A., and Hasselbrink, E. (1993) *J. Chem. Phys.*, **99**, 682.

125 Frischkorn, C. and Wolf, M. (2006) *Chem. Rev.*, **106**, 4207.

126 Wolf, M., Hotzel, A., Knoesel, E., and Velic, D. (1999) *Phys. Rev. B*, **59**, 5926.

127 Bisio, F., Winkelmann, A., Lin, W.C., Chiang, C.T., Nývlt, M., Petek, H., and Kirschner, J. (2009) *Phys. Rev. B*, **80**, 125432.

128 Cavalieri, A.L. *et al.* (2007) *Nature*, **449**, 1029.

129 Ueba, H. and Gumhalter, B. (2007) *Prog. Surf. Sci.*, **82**, 193.

130 Raether, H. (1988) *Surface Plasmons on Smooth and Rough Surfaces and on Gratings*, Springer, Berlin.

131 van de Hulst, H.C. (1981) *Light Scattering by Small Particles*, Dover Publications, New York.

132 Kreibig, U. and Vollmer, M. (1995) *Optical Properties of Metal Clusters*, Springer, Berlin.

133 Bohm, D. and Pines, D. (1953) *Phys. Rev.*, **92**, 609.

134 Pines, D. (1956) *Rev. Mod. Phys.*, **28**, 184.

135 Etchegoin, P.G., Le Ru, E.C., and Meyer, M. (2006) *J. Chem. Phys.*, **125**, 164705.

136 Etchegoin, P.G. and Le Ru, E.C. (2006) *J. Phys. Condens. Matter*, **18**, 1175.

137 McMahon, J.M., Gray, S.K., and Schatz, G.C. (2009) *Phys. Rev. Lett.*, **103**, 097403.

138 McMahon, J.M., Gray, S.K., and Schatz, G.C. (2009) *Phys. Rev. Lett.*, **103**, 097403.

139 Maier, S.A. (2007) *Plasmonics: Fundamentals and Applications*, Springer, New York.

140 Zayats, A.V., Smolyaninov, I.I., and Maradudin, A.A. (2005) *Phys. Rep.*, **408**, 131.

141 Barnes, W.L., Dereux, A., and Ebbesen, T.W. (2003) *Nature*, **424**, 824.

142 Pitarke, J.M., Silkin, V.M., Chulkov, E.V., and Echenique, P.M. (2007) *Rep. Prog. Phys.*, **70**, 1.

143 Jackson, J.D. (1999) *Classical Electrodynamics*, John Wiley & Sons, Inc., New York.

144 Klein, M.V. and Furtak, T.E. (1986) *Optics*, John Wiley & Sons, Inc., New York.

145 Ritchie, R.H. (1957) *Phys. Rev.*, **106**, 874.

146 Otto, A. (1968) *Z. Phys.*, **216**, 398.

147 Kretschmann, E. and Raether, H. (1968) *Z. Naturforsch. A*, **23A**, 2135.

148 Teng, Y.Y. and Stern, E.A. (1967) *Phys. Rev. Lett.*, **19**, 511.

149 Kubo, A., Pontius, N., and Petek, H. (2007) *Nano Lett.*, **7**, 470.

150 Hecht, B., Bielefeldt, H., Novotny, L., Inouye, Y., and Pohl, D.W. (1996) *Phys. Rev. Lett.*, **77**, 1889.

151 Renger, J., Quidant, R., van Hulst, N., and Novotny, L. (2010) *Phys. Rev. Lett.*, **104**, 046803.

152 Pendry, J.B., Martin-Moreno, L., and Garcia-Vidal, F.J. (2004) *Science*, **305**, 847.

153 Hibbins, A.P., Evans, B.R., and Sambles, J.R. (2005) *Science*, **308**, 670.

154 Bastard, G. (1988) *Wave Mechanics Applied to Semiconductor Heterostructures*, Halsted Press, New York.

155 Joannopoulos, J.D., Meade, R.D., and Winn, J.N. (1995) *Photonic Crystals: Molding the Flow of Light*, Princeton University Press, Princeton, NJ.

156 Pendry, J.B. (2000) *Phys. Rev. Lett.*, **85**, 3966.

157 Pendry, J.B., Schurig, D., and Smith, D.R. (2006) *Science*, **312**, 1780.

158 Sarid, D. (1981) *Phys. Rev. Lett.*, **47**, 1927.

159 Lamprecht, B., Krenn, J.R., Schider, G., Ditlbacher, H., Salerno, M., Felidj, N., Leitner, A., Aussenegg, F.R., and Weeber, J.C. (2001) *Appl. Phys. Lett.*, **79**, 51.

160 Berini, P. (1999) *Opt. Lett.*, **24**, 1011.

161 Berini, P. (2000) *Phys. Rev. B*, **61**, 10484.

162 Berini, P. (2001) *Phys. Rev. B*, **63**, 125417.

163 Kim, D.S. *et al.* (2003) *Phys. Rev. Lett.*, **91**, 143901.

164 Bergman, D.J. and Stockman, M.I. (2003) *Phys. Rev. Lett.*, **90**, 027402.

165 Oulton, R.F., Sorger, V.J., Zentgraf, T., Ma, R.M., Gladden, C., Dai, L., Bartal, G., and Zhang, X. (2009) *Nature*, **461**, 629.

166 Aigouy, L., Lalanne, P., Hugonin, J.P., Julié, G., Mathet, V., and Mortier, M. (2007) *Phys. Rev. Lett.*, **98**, 153902.

167 Meyer zu Heringdorf, F.J., Chelaru, L.I., Möllenbeck, S., Thien, D., and Horn-von Hoegen, M. (2007) *Surf. Sci.*, **601**, 4700.

168 Vesseur, E.J.R., de Waele, R., Lezec, H.J., Atwater, H.A., de Abajo, F.J.G., and Polman, A. (2008) *Appl. Phys. Lett.*, **92**, 083110.

169 Kubo, A., Onda, K., Petek, H., Sun, Z.J., Jung, Y.S., and Kim, H.K. (2005) *Nano Lett.*, **5**, 1123.

170 Stockman, M.I., Kling, M.F., Kleineberg, U., and Krausz, F. (2007) *Nat. Photonics*, **1**, 539.

171 Atwater, H.A. and Polman, A. (2010) *Nat. Mater.*, **9**, 205.

172 Willets, K.A. and Van Duyne, R.P. (2007) *Annu. Rev. Phys. Chem.*, **58**, 267.

173 Kim, K.H., Watanabe, K., Mulugeta, D., Freund, H.-J., and Menzel, D. (2011) *Phys. Rev. Lett.*, **107**, 047401.

174 Bohren, C.F. and Huffman, D.R. (1983) *Absorption and Scattering of Light by Small Particles*, John Wiley & Sons, Inc., New York.

175 Novotny, L. and Hecht, B. (2006) *Principles of Nano-Optics*, Cambridge University Press, Cambridge.

176 Jackson, J.D. (1999) *Classical Electrodynamics*, John Wiley & Sons, Inc., New York.

177 Muller, J., Sonnichsen, C., von Poschinger, H., von Plessen, G., Klar, T.A., and Feldmann, J. (2002) *Appl. Phys. Lett.*, **81**, 171.

178 Boyer, D., Tamarat, P., Maali, A., Lounis, B., and Orrit, M. (2002) *Science*, **297**, 1160.

179 Klar, T., Perner, M., Grosse, S., von Plessen, G., Spirkl, W., and Feldmann, J. (1998) *Phys. Rev. Lett.*, **80**, 4249.

180 Lindfors, K., Kalkbrenner, T., Stoller, P., and Sandoghdar, V. (2004) *Phys. Rev. Lett.*, **93**, 037401.

181 Arbouet, A., Christofilos, D., Del Fatti, N., Vallee, F., Huntzinger, J.R., Arnaud, L., Billaud, P., and Broyer, M. (2004) *Phys. Rev. Lett.*, **93**, 127401.

182 van Dijk, M.A., Lippitz, M., and Orrit, M. (2005) *Phys. Rev. Lett.*, **95**, 267406.

183 Muskens, O.L., Billaud, P., Broyer, M., Fatti, N., and Vallee, F. (2008) *Phys. Rev. B*, **78**, 205410.

184 Kubo, A., Jung, Y.S., Kim, H.K., and Petek, H. (2007) *J. Phys. B*, **40**, S259.

185 Munzinger, M., Wiemann, C., Rohmer, M., Guo, L., Aeschlimann, M., and Bauer, M. (2005) *New J. Phys.*, **7**, 1.

186 Meier, M. and Wokaun, A. (1983) *Opt. Lett.*, **8**, 581.

187 Kuwata, H., Tamaru, H., Esumi, K., and Miyano, K. (2003) *Appl. Phys. Lett.*, **83**, 4625.

188 Heilweil, E.J. and Hochstrasser, R.M. (1985) *J. Chem. Phys.*, **82**, 4762.

189 Sonnichsen, C., Franzl, T., Wilk, T., von Plessen, G., Feldmann, J., Wilson, O., and Mulvaney, P. (2002) *Phys. Rev. Lett.*, **88**, 077402.

190 Sonnichsen, C., Franzl, T., Wilk, T., von Plessen, G., and Feldmann, J. (2002) *New J. Phys.*, **4**, 93.1–93.8.

191 Hu, M., Novo, C., Funston, A., Wang, H.N., Staleva, H., Zou, S.L., Mulvaney, P., Xia, Y.N., and Hartland, G.V. (2008) *J. Mater. Chem.*, **18**, 1949.

192 Stietz, F., Bosbach, J., Wenzel, T., Vartanyan, T., Goldmann, A., and Trager, F. (2000) *Phys. Rev. Lett.*, **84**, 5644.

193 Baida, H. *et al.* (2009) *Nano Lett.*, **9**, 3463.

194 Pustovit, V.N. and Shahbazyan, T.V. (2006) *Chem. Phys. Lett.*, **420**, 469.

195 Kawabata, A. and Kubo, R. (1966) *J. Phys. Soc. Jpn.*, **21**, 1765.

196 Yannouleas, C. and Broglia, R.A. (1992) *Ann. Phys.*, **217**, 105.

197 Hovel, H., Fritz, S., Hilger, A., Kreibig, U., and Vollmer, M. (1993) *Phys. Rev. B*, **48**, 18178.

198 Deutsch, B., Hillenbrand, R., and Novotny, L. (2010) *Nano Lett.*, **10**, 652.

199 Ghenuche, P., Cherukulappurath, S., Taminiau, T.H., van Hulst, N.F., and Quidant, R. (2008) *Phys. Rev. Lett.*, **101**, 116805.

200 Sadiq, D., Shirdel, J., Lee, J.S., Selishcheva, E., Park, N., and Lienau, C. (2011) *Nano Lett.*, **11**, 1609.

201 Ropers, C., Solli, D.R., Schulz, C.P., Lienau, C., and Elsaesser, T. (2007) *Phys. Rev. Lett.*, **98**, 043907.

202 Vesseur, E.J.R., de Waele, R., Kuttge, M., and Polman, A. (2007) *Nano Lett.*, **7**, 2843.

203 Nelayah, J. *et al.* (2007) *Nat. Phys*, **3**, 348.

204 Wood, R.W. (1902) *Philos. Mag.*, **3**, 15.

205 Wood, R.W. (1935) *Phys. Rev.*, **48**, 928.

206 Fano, U. (1941) *J. Opt. Soc. Am.*, **31**, 213.

207 Ebbesen, T.W., Lezec, H.J., Ghaemi, H.F., Thio, T., and Wolff, P.A. (1998) *Nature*, **391**, 667.

208 Bethe, H.A. (1944) *Phys. Rev.*, **66**, 163.

209 Bouwkamp, C.J. (1954) *Rep. Prog. Phys.*, **17**, 35.

210 Hohng, S.C. (2002) *et al. Appl. Phys. Lett.*, **81**, 3239.

211 Krishnan, A., Thio, T., Kima, T.J., Lezec, H.J., Ebbesen, T.W., Wolff, P.A., Pendry, J., Martin-Moreno, L., and Garcia-Vidal, F.J. (2001) *Opt. Commun.*, **200**, 1.

212 Ghaemi, H.F., Thio, T., Grupp, D.E., Ebbesen, T.W., and Lezec, H.J. (1998) *Phys. Rev. B*, **58**, 6779.

213 Ropers, C., Park, D.J., Stibenz, G., Steinmeyer, G., Kim, J., Kim, D.S., and Lienau, C. (2005) *Phys. Rev. Lett.*, **94**, 113901.

214 Sarrazin, M., Vigneron, J.P., and Vigoureux, J.M. (2003) *Phys. Rev. B*, **67**, 085415.

215 Genet, C., van Exter, M.P., and Woerdman, J.P. (2003) *Opt. Commun.*, **225**, 331.

216 Cohen-Tannoudji, C., Dupont-Roc, J., and Grynberg, G. (1992) *Atom-Photon Interactions: Basic Processes and Applications*, John Wiley & Sons, Inc., New York.

217 Scully, M.O. and Zubairy, M.S. (1997) *Quantum Optics*, Cambridge University Press, Cambridge.

218 Dicke, R.H. (1954) *Phys. Rev.*, **93**, 99.

219 Garcia-Vidal, F.J., Martin-Moreno, L., Ebbesen, T.W., and Kuipers, L. (2010) *Rev. Mod. Phys.*, **82**, 729.

220 Martin-Moreno, L., Garcia-Vidal, F.J., Lezec, H.J., Pellerin, K.M., Thio, T., Pendry, J.B., and Ebbesen, T.W. (2001) *Phys. Rev. Lett.*, **86**, 1114.

221 Lochbihler, H. (1994) *Phys. Rev. B*, **50**, 4795.

222 Lee, K.G. and Park, Q.H. (2005) *Phys. Rev. Lett.*, **95**, 103902.

223 Muller, R., Malyarchuk, V., and Lienau, C. (2003) *Phys. Rev. B*, **68**, 205415.

224 Muller, R., Ropers, C., and Lienau, C. (2004) *Opt. Express*, **12**, 5067.

225 Lezec, H.J., Degiron, A., Devaux, E., Linke, R.A., Martin-Moreno, L., Garcia-Vidal, F.J., and Ebbesen, T.W. (2002) *Science*, **297**, 820.

226 Tegenfeldt, J.O. *et al.* (2001) *Phys. Rev. Lett.*, **86**, 1378.

227 Neacsu, C.C., Berweger, S., Olmon, R.L., Saraf, L.V., Ropers, C., and Raschke, M.B. (2010) *Nano Lett.*, **10**, 592.

228 Berweger, S., Atkin, J.M., Xu, X.G., Olmon, R.L., and Raschke, M.B. (2011) *Nano Lett.*, **11**, 4309–4313.

229 Ropers, C., Neacsu, C.C., Elsaesser, T., Albrecht, M., Raschke, M.B., and Lienau, C. (2007) *Nano Lett.*, **7**, 2784.

230 Babadjanyan, A.J., Margaryan, N.L., and Nerkararyan, K.V. (2000) *J. Appl. Phys.*, **87**, 3785.

231 Cohen-Tannoudji, C., Diu, B., and Laloë, F. (1977) *Quantum Mechanics*, John Wiley & Sons, Inc., New York.

232 Stockman, M.I., Bergman, D.J., Anceau, C., Brasselet, S., and Zyss, J. (2004) *Phys. Rev. Lett.*, **92**, 057402.

233 Kurihara, K., Yamamoto, K., Takahara, J., and Otomo, A. (2008) *J. Phys. A*, **41**, 295401.

234 Durach, M., Rusina, A., Stockman, M.I., and Nelson, K. (2007) *Nano Lett.*, **7**, 3145.

235 Issa, N.A. and Guckenberger, R. (2007) *Plasmonics*, **2**, 31.

236 Gramotnev, D.K., Vogel, M.W., and Stockman, M.I. (2008) *J. Appl. Phys.*, **104**, 034311.

237 Baida, F.I. and Belkhir, A. (2009) *Plasmonics*, **4**, 51.

238 Gramotnev, D.K. (2005) *J. Appl. Phys.*, **98**, 104302.

239 Verhagen, E., Kuipers, L., and Polman, A. (2007) *Nano Lett.*, **7**, 334.

240 Verhagen, E., Spasenovic, M., Polman, A., and Kuipers, L. (2009) *Phys. Rev. Lett.*, **102**, 203904.

241 Knox, R.S. (1963) *Theory of Excitons*, Academic Press, New York.

242 Yu, P. (2010) *Fundamentals of Semiconductors: Physics and Materials Properties*, Springer, New York.

243 Haug, H. and Koch, S.W. (2009) *Quantum Theory of the Optical and Electronic Properties of Semiconductors*, World Scientific.

244 Davydov, A.S. (1971) *Theory of Molecular Excitons*, Plenum Press, New York.

245 Kobayashi, T. (1996) *J-Aggregates*, World Scientific, Singapore.

246 Olaya-Castro, A. and Scholes, G.D. (2011) *Int. Rev. Phys. Chem.*, **30**, 49.

247 Biolatti, E., Iotti, R.C., Zanardi, P., and Rossi, F. (2000) *Phys. Rev. Lett.*, **85**, 5647.

248 Unold, T., Mueller, K., Lienau, C., Elsaesser, T., and Wieck, A.D. (2005) *Phys. Rev. Lett.*, **94**, 137404.

249 Prodan, E., Radloff, C., Halas, N.J., and Nordlander, P. (2003) *Science*, **302**, 419.

250 Wang, Z.L. and Cowley, J.M. (1987) *Ultramicroscopy*, **23**, 97.

251 Garcia de Abajo, F.J. and Howie, A. (2002) *Phys. Rev. B*, **65**, 115418.

252 Prodan, E. and Nordlander, P. (2004) *J. Chem. Phys.*, **120**, 5444.

253 Nordlander, P., Oubre, C., Prodan, E., Li, K., and Stockman, M.I. (2004) *Nano Lett.*, **4**, 899.

254 Fofang, N.T., Park, T.H., Neumann, O., Mirin, N.A., Nordlander, P., and Halas, N.J. (2008) *Nano Lett.*, **8**, 3481.

255 Lidzey, D.G., Bradley, D.D.C., Armitage, A., Walker, S., and Skolnick, M.S. (2000) *Science*, **288**, 1620.

256 Vasa, P. *et al.* (2010) *ACS Nano*, **4**, 7559.

257 Wiederrecht, G.P., Wurtz, G.A., and Hranisavljevic, J. (2004) *Nano Lett.*, **4**, 2121.

258 Bellessa, J., Bonnand, C., Plenet, J.C., and Mugnier, J. (2004) *Phys. Rev. Lett.*, **93**, 036404.

259 Dintinger, J., Klein, S., Bustos, F., Barnes, W.L., and Ebbesen, T.W. (2005) *Phys. Rev. B*, **71**, 035424.